Numerical Simulation of Extreme Waves During the Storm of 20–22 January 2000 Using Winds Generated by the CMC Weather Prediction Model

Roop Lalbeharry[1,*], Ralph Bigio[2], Bridget R. Thomas[3] and Laurence Wilson[4]

[1]*Environmental Numerical Weather Prediction Research Section, Science and Technology Branch*
Environment Canada
4905 Dufferin Street, Toronto, ON M3H 5T4
[2]*Weather Services Centre Comox, CFB Comox*
Lazo, BC
[3]*Climate Data and Analysis Section, Science and Technology Branch*
Environment Canada
Dartmouth, NS
[4]*Atmospheric Numerical Weather Prediction Research Section, Science and Technology Branch*
Environment Canada
Dorval, QC

[Original manuscript received 27 March 2007; accepted 29 September 2008]

ABSTRACT *The storm of 20–22 January 2000 over Canada's Atlantic Provinces was an exceptional storm for several reasons, these include extremely high coastal ocean waves, widespread coastal damage due to the storm surge, very strong winds over a large area, an extremely fast deepening rate, and a very low central pressure. It produced unusually large waves which caused significant damage in communities along the south coast of Newfoundland and the eastern shores of Nova Scotia. Bottom scouring was observed around the feet of three mobile offshore oil and gas drilling platforms operating near Sable Island. Using buoy data enhanced with a detailed data set from one of the platforms, this study examines the growth of destructive waves and the performance of two state-of-the-art third generation ocean wave models running in shallow water mode.*

The wave models perform well in numerically simulating the extreme waves associated with this storm. They correctly predict the growth of wind waves and handle the arrival of long-period swells well. Unprecedented waves that damaged buildings and a lighthouse in the Channel Head area of Port-Aux-Basques retained most of their deep-water energy until they were less than one wavelength from the beach. Computations show that dynamic (or trapped) fetch was not a contributing factor in the generation of the observed extreme sea states although the long-period swells were supported by winds for a significant part of their transit northward. However, it appears that the model-generated enhanced wave growth at the buoy location just off the southwestern coast of Newfoundland may be partially linked to the creation of model trapped fetch. The January 2000 storm was indeed an extreme storm and was the most intense non-tropical storm to form over Atlantic Canada in decades.

RÉSUMÉ *[Traduit par la rédaction] La tempête qui a eu lieu du 20 au 22 janvier dans les provinces atlantiques du Canada était exceptionnelle à bien des égards, notamment en raison des vagues océaniques côtières extrêmement hautes, des dommages étendus le long des côtes causés par l'onde de tempête, des vents très forts dans une vaste région, un taux de creusement extrêmement rapide et une pression centrale très basse. Elle a produit des vagues exceptionnellement hautes qui ont causé des dommages importants dans les communautés situées le long de la côte sud de Terre-Neuve et de la côte est de la Nouvelle-Écosse. Un affouillement de fond a été observé autour des pieds de trois plates-formes mobiles de forage pétrolier et gazier en mer installées près de l'île de Sable. En utilisant des données de bouée complétées par un ensemble de données détaillées de l'une des plates-formes, cette étude examine la croissance des vagues destructrices de même que les résultats de deux modèles de vagues océaniques de troisième génération à la fine pointe fonctionnant en mode d'eau peu profonde.*

Les modèles de vagues fonctionnent bien en simulant de façon numérique les vagues extrêmes associées à cette tempête. Ils prévoient correctement la croissance de la mer du vent et traitent bien l'arrivée des houles de longue période. Les vagues sans précédent qui ont endommagé des bâtiments et un phare dans la zone de Channel Head à Port-Aux-Basques ont conservé la plus grande partie de leur énergie en eau profonde jusqu'à ce qu'elles soient à moins d'une longueur d'onde de la plage. Les calculs montrent que le fetch dynamique (ou emprisonné) n'a pas contribué à la formation des états de la mer extrêmes observés, même si les houles de longue période étaient soutenues par le vent sur une partie importante de leur parcours vers le nord. Cependant, il semble que la croissance accrue des vagues proposée par le modèle à l'emplacement de la bouée juste au large de la côte sud-ouest de Terre-Neuve soit en partie liée à la création par le modèle d'un fetch emprisonné. La tempête de janvier 2000 était de fait une tempête extrême et a été la tempête non tropicale la plus intense à se former dans le Canada atlantique depuis des décennies.

*Corresponding author's e-mail: Roop.Lalbeharry@ec.gc.ca

1 Introduction

On 20 January 2000 a low pressure centre formed south of Cape Hatteras. This low, hereinafter referred to as the 'superbomb', deepened explosively (42 hPa in 24 hours, 49 hPa in 30 hours) reaching a minimum central pressure of 946 hPa at 18:00 UTC on 21 January south of Nova Scotia (NS). Perrie et al. (2005) describe the dynamics supporting the development of this 'superbomb', so called because it deepened much more rapidly than a typical 'bomb' (defined as having a central pressure that falls at a rate of least 1 hPa h^{-1} for 24 hours (Sanders and Gyakum, 1980)). Late on 21 January, it turned north, crossed eastern NS and moved into the Gulf of St. Lawrence. On 22 January it weakened and moved through eastern Quebec into Labrador. Figure 1 shows the analyzed track of the storm centre through the East Coast buoy array every six hours from the Atlantic Storm Prediction Centre (ASPC), along with the corresponding weather prediction model storm track obtained from 00H forecasts from the Canadian Meteorological Centre (CMC). Also shown in Fig. 1 are the locations of the validation buoys and their corresponding World Meteorological Organization (WMO) identification numbers, the mobile offshore drilling platform Rowan Gorilla III (RG3) and the town of Port-aux-Basques (PAB), Newfoundland.

In Atlantic Canada coastal communities were severely affected by waves, winds, storm surge, and sea ice (Forbes et al., 2000; MacPhee, unpublished manuscripts). There was damage to wharfs, roads, breakwaters, and other coastal infrastructure in many areas of Atlantic Canada, including the Fundy Shore of NS, the eastern shore of mainland NS and Cape Breton Island, the south coast of Newfoundland, many coastal areas of Prince Edward Island (PEI), and the eastern shore of New Brunswick (NB). A record high storm surge of 1.4 m occurred at Charlottetown, PEI, which coincided with high tide and caused widespread flooding. The storm caused extensive sea-ice ride-up and pileup onshore in PEI and NB and damage to homes and wharves. The hurricane force winds and heavy snowfall that accompanied the storm caused blizzard conditions that closed highways. The winds also initiated a large storm surge on which damaging waves were superimposed. This storm surge and a comparison with climatology are described by Parkes and Ketch (2002) and Thompson et al. (2002). Bobanovic et al. (2006) describe the synoptic pattern and the wind forcing and modelling of the storm surge.

At Channel Head near Port-Aux-Basques, Newfoundland, there was damage to residential, commercial and municipal buildings, including a lighthouse. MacPhee (unpublished manuscript) described the unprecedented wave damage in the Channel Head area in detail and found that two particularly large waves struck during the early hours of 22 January 2000, the first arriving at approximately 06:30 UTC and the second approximately ten minutes later. At this location the modelled storm surge was approximately 0.8 m (Bobanovic et al., 2006) but the actual damage was primarily wave related. The damage to this community from these two waves and to other communities along the south coast of Newfoundland was estimated to be about \$4.7 million. Relief was made available through approved disaster relief funding to repair storm damage to municipal infrastructure and personal property.

Three mobile offshore oil and gas drilling platforms were operating near Sable Island when this storm approached. Due to the forecast of extremely high winds and waves, RG3 at the Cohasset-Panuke site and the Rowan Gorilla II at the Venture site were completely evacuated while most of the staff were evacuated from the Santa Fe Galaxy II at the Thebaud site leaving only essential personnel. All the rigs had to be repositioned due to shifting and settling in sand around their legs from wind and wave action (Borgel, 2001).

The analyzed minimum central pressure of 946 hPa by the ASPC at 18:00 UTC on 21 January when the low was centred south of NS was the deepest pressure produced by any storm that had affected Atlantic Canada in decades (Borgel, 2001). The rarity of such an intense storm occurring over Atlantic Canada was also assessed by W. Richards (2002, personal communication) who found a return period of 30 years for storm intensities ranging from 948 hPa to 956 hPa at several locations in this region. The corresponding CMC Global Environmental Multiscale (GEM) weather prediction model central pressure of 950 hPa shown in Fig. 2 compares reasonably well with the analyzed value of 946 hPa.

The main objectives of this study are 1) to assess how well the wave models perform in generating the extreme sea state associated with this superbomb given the wind forcing available during the storm passage, 2) to consider whether dynamic fetch played any role in the development of these waves, and 3) to look at the storm in the context of the wave climate for the area. The organization of this paper is as follows, Section 2 presents a brief description of the wave models used in this study and their primary inputs, Section 3 briefly reviews the theory of limiting wave steepness, Section 4 describes the sources of the wave data, Section 5 presents the results and provides some discussion. The wave climate context for this storm for the Scotian Shelf is described in Section 6, followed by a summary and conclusions in Section 7.

2 The wave models

a *Action Density Balance Equation*

The ocean waves are described with the two-dimensional wave action density spectrum $N(\sigma,\theta,\phi,\lambda,t)$ as a function of relative angular frequency σ, wave direction θ (measured clockwise relative to true north), latitude ϕ, longitude λ, and time t. Here, $\sigma = [(gk)\tanh(kh)]^{1/2}$ where k (= $2\pi/L$, L being the wavelength) is the wave number, g is acceleration due to gravity, and h is the water depth. The action density spectrum is defined as the energy density spectrum $F(\sigma,\theta,\phi,\lambda,t)$ divided by σ observed in a frame moving with the ocean current velocity, that is, $N(\sigma,\theta,\phi,\lambda,t) = F(\sigma,\theta,\phi,\lambda,t)/\sigma$. The action density is chosen because it is conserved in the presence of time-dependent water depths and currents whereas the energy density spectrum is not. In general, the conservation equation

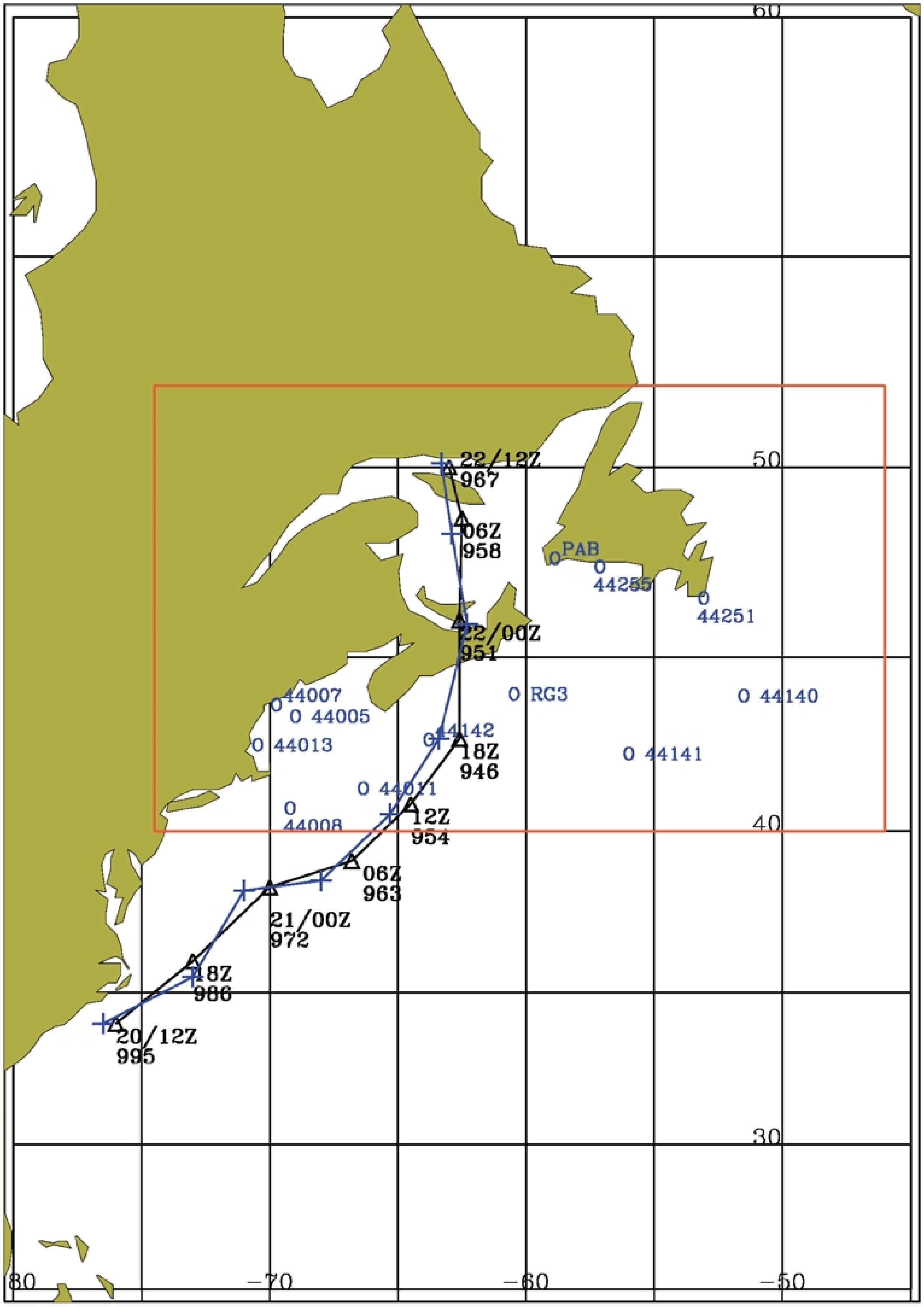

Fig. 1 Storm tracks at six-hour intervals for the period 20–22 January 2000. The observed track is given by the solid black line with the symbol "Δ" with the lower number being the observed central pressure in hPa. The solid blue line with the symbol "+" is the CMC GEM regional model 00H forecast track. The box enclosed by a red line is the area covered by the nested fine 0.1° × 0.1° grid lying between 40.0°N – 52.0°N and 74.5°W – 46.0°W. The locations of the buoys used for validation relative to the storm track and their corresponding WMO identification numbers are also shown. RG3 is the drilling platform called 'Rowan Gorilla III' and PAB marks the location of Port-aux-Basques.

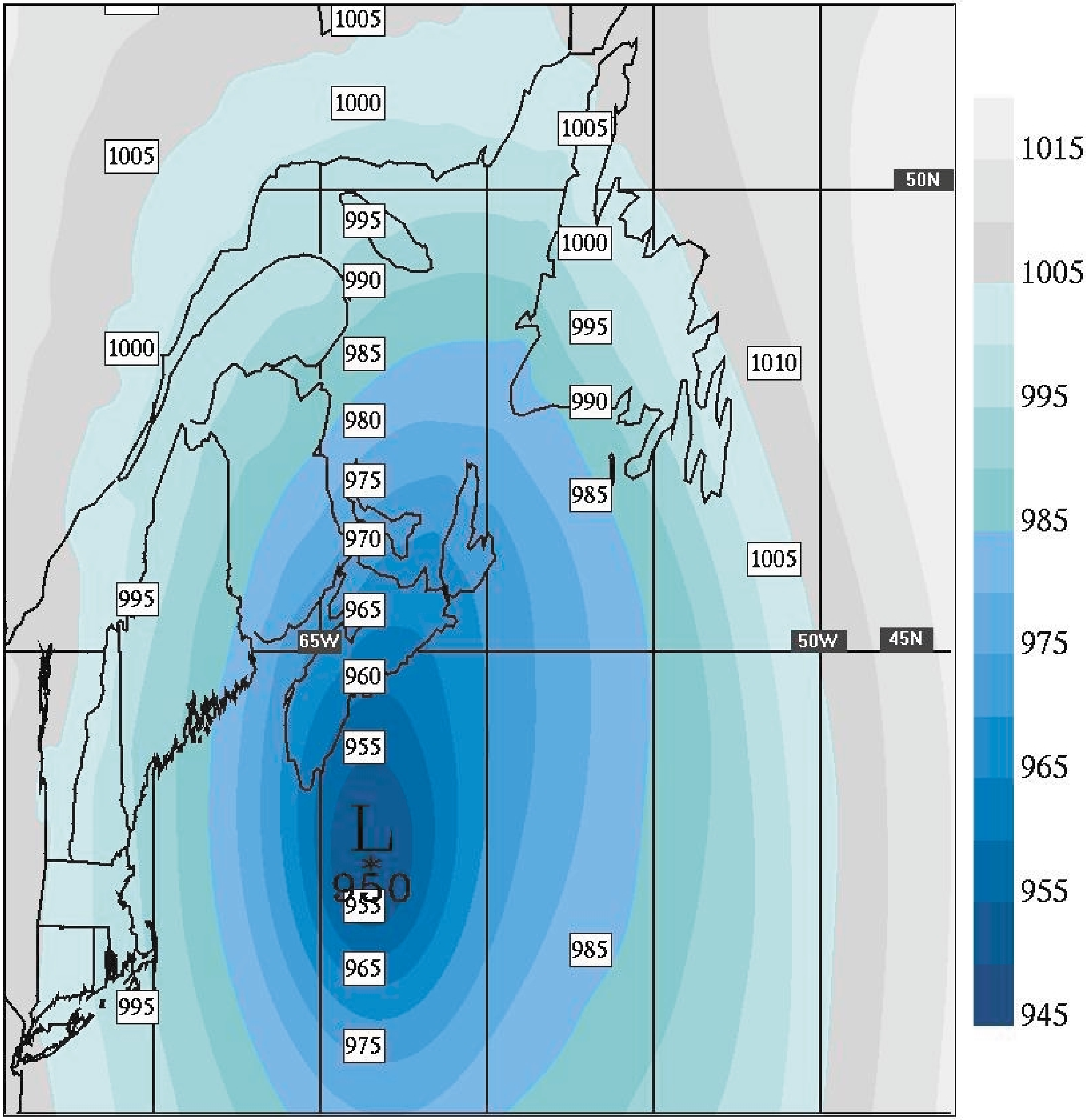

Fig. 2 CMC GEM weather prediction model 00H forecast of the mean sea level pressure (MSLP) valid at 18:00 UTC 21 January 2000 in which the colour contours indicate pressure in hPa. The model minimum central pressure is 950 hPa while the corresponding analyzed pressure is 946 hPa.

for N in flux form in spherical coordinates and in frequency-direction space is governed by the transport equation given in the form:

$$\frac{\partial N}{\partial t}+(\cos\phi)^{-1}\frac{\partial}{\partial\varphi}\left(c_\varphi\cos\phi N\right)+\frac{\partial}{\partial\lambda}\left(c_\lambda N\right)+\frac{\partial}{\partial\sigma}\left(c_\sigma N\right)+\frac{\partial}{\partial\theta}\left(c_\theta N\right)=\frac{S}{\sigma} \tag{1}$$

where

$$S = S_{phil}+S_{in}+S_{nl4}+S_{ds}+S_{bf}. \tag{2}$$

In Eq. (1) the first term on the left-hand side represents the local rate of change of action density in time. The second and third terms represent the propagation of action density in geographical space (with propagation velocities c_ϕ and c_λ in latitudinal and longitudinal directions, respectively). The fourth term gives the shifting of the relative frequency due to variations in depth and current (with propagation velocity c_σ in σ space) and the fifth term the depth-induced and current-induced refraction (with propagation velocity c_θ in θ space). For zero current and time-independent depth $c_\sigma = 0$, Eq. (1) reduces to the energy balance equation, that is, the fourth term on the left-hand side vanishes and the depth refraction term (fifth term) depends only on the depth gradient.

The term $S = S(\sigma,\theta,\phi,\lambda,t)$ on the right-hand side of Eq. (1) is the net source term expressed in terms of energy density. It is the sum of a number of source terms given in Eq. (2) representing the effects of wave generation by wind (S_{phil} and S_{in}), quadruplet non-linear wave-wave interactions (S_{nl4}), dissipation due to whitecapping (S_{ds}) and bottom friction (S_{bf}). The linear wind growth term S_{phil} is from Cavaleri and Malonette-Rizzoli (1981) but with a filter to eliminate contributions from frequencies lower than the Pierson-Moskowitz frequency (Tolman, 1992) and is hereinafter referred as CR81. The term S_{in} is the exponential wind growth source term based on the formulations of Komen et al. (1984) and Janssen (1989, 1991). The source term S_{nl4} is the quadruplet non-linear wave-wave interaction which transfers energy from spectral peaks to lower and higher frequencies. The energy is redistributed so that there is no net loss or gain of energy due to non-linear wave-wave interactions. The S_{nl4} term dominates the evolution of the spectrum in deep and intermediate waters and is computed with the discrete interaction approximation method of Hasselmann et al. (1985). The bottom friction source term S_{bf} is based on the empirical Joint North Sea Wave Project (JONSWAP) model of Hasselmann et al. (1973) with the friction dissipation constant in S_{bf} being a tunable parameter set to 0.038 $m^2\ s^{-3}$ in this study.

b *The WAM4.5*

The WAve Model (WAM) solves the energy balance form of Eq. (1) for zero current and fixed water depth on a spherical grid and in frequency-direction space. The Wave Model Development and Implementation (WAMDI) Group (WAMDI Group, 1988) describes the Cycle-3 version of WAM (hereinafter referred as WAM3) in which S_{in} and S_{ds} are based on the formulations of Komen et al. (1984). In the WAM Cycle-4 version (hereinafter referred as WAM4), S_{in} and S_{ds} are based on the formulations of Janssen (1989, 1991) in which the winds and waves are coupled, that is, there is a feedback of growing waves on the wind profile. The effect of this feedback is to enhance the wave growth of younger wind seas over that of older wind seas for the same wind. WAM4.5 is an update of WAM4 and incorporates many of the changes described in Monbaliu et al. (2000). It uses the first order upwind explicit propagation scheme, which results in the propagation time step being limited by the Courant-Friedrichs-Levy (CFL) condition, and a fully implicit source term integration scheme. The latter enhancement allows the specification of the source term integration time step to be larger than the propagation time step. To ensure that WAM remains numerically stable, a limitation on wave growth is imposed. This limiter is based on the formulation of Hersbach and Janssen (1999), hereinafter referred as HJ99, and gives the maximum total change of energy density per iteration per spectral wave component. It is expressed as

$$|\Delta F(f,\theta)|_{max} = 3.0 \times 10^{-7} g u_* f^{-4} f_c \Delta t \tag{3}$$

where f is the frequency, u_* the friction velocity, f_c the model prognostic cutoff frequency, and Δt the source term integration time step. Here $u_* = \max(u_*, g f^*_{PM}/f)$ and $f^*_{PM} = 5.6 \times 10^{-3}$ is the dimensionless Pierson-Moskowitz frequency. In terms of action density and σ, Eq. (3) can be expressed as

$$|\Delta N(\sigma,\theta)|_{max} = (2\pi)^2 \times 3.0 \times 10^{-7}\ g u_* \sigma_c \Delta t/(\sigma^3 k). \tag{4}$$

The source term S_{phil} based on CR81 has now been added to WAM4.5 as it was excluded in earlier versions of WAM. More details of the formulation of WAM can be found in Komen et al. (1994).

c *SWAN*

The Simulation of WAves Nearshore (SWAN) model solves the action balance equation on a spherical grid and in σ-θ space. Because of the assumptions of time-independent water depth and no current, the solution of Eq. (1) is equivalent to the solution of the energy balance equation as in WAM4.5. The propagation scheme is fully implicit and for the source term integration scheme the fully implicit option is chosen. SWAN has the option of using WAM3 or WAM4 physics for the S_{in} and S_{ds} source terms with the default option being WAM3. The wind input term in Eq. (2) includes S_{phil}. The wave growth limiter used in SWAN is described in Ris (1997) and is hereinafter referred to as R97, and is given by

$$|\Delta N(\sigma,\theta)|_{max} = (0.1\alpha_{PM})/(2\sigma k^3 c_g) \tag{5}$$

where $\alpha_{PM} = 0.0081$ is Phillips' constant. The SWAN implementation of WAM4 is not consistent with the actual implementation of WAM4. The shift growth parameter $z_\alpha = 0.011$ in S_{in} is omitted and the limiter R97 is used instead of HJ99. The modified S_{in} now includes z_α and a new subroutine is added so that when the WAM4 option is used, the limiter HJ99 is called. The model results so produced are now in better agreement with those from WAM4.5 and WAM3. The version of SWAN used in this study is SWAN Cycle-III version 40.31 in which the model is run in the nonstationary mode. This version is a parallelized version with Message-Passing Interface (MPI) as an option which considerably reduces the model run time compared to the non-parallelized version. More details of SWAN are given in Booij et al. (1999) and Ris et al. (1999). The documentation of version 40.31 used in this study is described in SWAN (2004).

d *Model Setup*

WAM4.5 and SWAN are used to simulate wave heights for the superbomb. Simulations using these models are performed on two grids, a coarse grid with a resolution of 0.5° covering the area 25°N–70°N and 82°W–0° and a fine grid with a resolution of 0.1° nested within the coarse grid and covering the area 40°N–52°N and 74.5°W–46°W, the boundaries of which are shown by the solid red lines in Fig. 1.

WAM4.5 runs on the coarse grid while the SWAN model and a nested version of the WAM4.5 run on the fine grid using the boundary conditions provided by the coarse grid WAM4.5. The solution of Eq. (1) is provided for 25 frequencies logarithmically spaced from 0.042 Hz to 0.41 Hz at intervals of $\delta f/f = 0.1$ and 24 directional bands of 15° each measured clockwise from true north. In the numerical representation of the spectrum the directional bins are rotated by half the beam width to avoid propagation of spurious waves along latitude or longitude (Bidlot et al., 2002), that is, the first bin is centred at 7.5° and the last bin at 352.5°. Both models run in shallow water mode in which the bottom friction source term is activated. In finite water depth the wave energy propagates with the group velocity $c_g = c/2[1 + 2kh/\sinh(kh)]$ where $c = [(g/k)\tanh(kh)]^{½}$ is the phase speed, For deep water ($h > L/4$) $c_g = c/2$, $c = g/(2\pi f)$ and $L = 1.56T^2$ m where T is the wave period in seconds. For shallow water ($h < L/25$) $c_g = c = (gh)^{½}$ in which both the group and phase velocities are functions only of the water depth. As the waves move from deep to intermediate and shallow waters, the wave height increases due to shoaling but after this initial rise the height decreases as wave energy is lost to bottom friction.

The results of five different model runs are presented in this study, namely, two for WAM4.5 and three for SWAN. These five runs are identified as (1) WAM45-CG for the WAM4.5 coarse grid run, (2) WAM45-FG for the WAM4.5 fine grid run, (3) SWN-WAM3 for the SWAN run using WAM3 (Komen) physics, (4) SWN-WAM4 for the SWAN run using WAM4 (Janssen) physics as implemented in SWAN, and (5) SWN-WAM4+ for the run using the modified implementation of SWAN WAM4 physics. Table 1 summarizes the source term and wave growth limiter options, the propagation and source term integration numerical schemes, time steps and the spatial and spectral grid resolutions used in the two runs of WAM4.5 and the three runs of the SWAN.

e *Model Inputs*

The primary inputs to the two models are the bathymetry, the wind forcing and the ice field. The bathymetry for the fine grid is shown in Fig. 3 in which water depth varies from a minimum of 5 m to a maximum of 999 m. Water depth less than 5 m is set to 5 m and that greater than 999 m to 999 m. The Laurentian Channel is clearly visible with a maximum water depth of 536 m.

The two models are forced by the 10 m surface winds obtained from the CMC regional GEM weather prediction model at three-hour intervals. The wind dataset is created by assembling the 00, 03, 06 and 09 forecast hour winds of the 00:00 UTC and 12:00 UTC daily runs of the GEM model to produce a quasi-hindcast dataset for the storm simulation period 17–23 January 2000. The winds are first generated on the GEM model grid and then interpolated onto the wave model coarse and fine grids, respectively. The same fine grid wind field drives both the nested WAM4.5 and SWAN. For each run the model is spun up for the first two days of the simulation period to create model initial states, following which the model outputs are then evaluated against observations. Ice is not a factor in this study since there are no ice points in the area of interest traversed by the storm.

3 Brief review of limiting wave steepness

The local wave steepness, defined as $S_S = H/L$ where H is the wave height, limits the growth of waves. Once S_S reaches some critical limit, a further transfer of energy causes the waves to become unstable and to spill and plunge forward resulting in significant loss of energy. According to Stokes theory the critical wave steepness is $S_{crit} = 1/7$ but for real ocean waves it seldom reaches 1/10 (WMO, 1998). The limiting value is constant, that is, $H_{lim}/L = S_{crit} = K$. For deep water waves $L = gT^2/(2\pi)$ so that $S_S = 2\pi H/(gT^2)$ and $H_{lim}/T^2 = K/(2\pi)g$. Buckley (1988) used archived buoy data from the National Data Buoy Center (NDBC) of the National Oceanic and Atmospheric Administration (NOAA) and plotted extreme values of significant wave height H_s and the corresponding T_p to define an envelope of extreme combinations of peak H_s denoted as H_{lim} and the corresponding peak period T_p. He obtained an empirical value of 0.00776 for $K/(2\pi)$ giving the equation

$$H_{lim}/T_p^{\ 2} = 0.00776g \tag{6}$$

and the limiting significant wave steepness value for ocean waves $K = 0.049$, or about 1/20. Equation (6) establishes a parametric boundary above which the waves become unstable. An application of the H_s steepness limit in the context of storm climatology is discussed in Section 6.

4 Wave data sources

The buoys used in this study for evaluation of model results are shown in Fig. 1. Those with WMO identification numbers 44005, 44007, 44008, 44011 and 44013 are owned and operated by NOAA's NDBC, while those with numbers 44140, 44141, 44142, 44251 and 44255 are owned and operated by the Meteorological Service of Canada (MSC) of Environment Canada, but the data are archived by the Marine Environmental Data Service (MEDS) now called Integrated Science Data Management (ISDM) of the Department of Fisheries and Ocean. However, in this study the more familiar acronym MEDS is used to refer to the archived data. The buoy identified as RG3 is a Datawell waverider operated by COA Coastal Associates Inc. (hereinafter referred to as COA; acquired in 2006 by AMEC Earth and Environmental Ltd., a division of AMEC), Dartmouth, NS. The buoys are all nondirectional with their names, hull configurations and water depths given in Table 2. The 3 m discus buoy has a circular hull, the 6 m Navy Oceanographic and Meteorological Automated Device (NOMAD) buoy a ship-shaped hull, and the Datawell waverider a spherical hull with a hull diameter of 0.9 m. Because too few observations were available from buoy 44251 during the passage of the storm, it is not included

TABLE 1. Source term and wave growth limiter options, propagation and source term integration numerical schemes, time steps and grid resolutions used in the two runs of WAM4.5 and the three runs of SWAN.

Source term/ Limiter/Other	Physics	WAM4.5		SWAN		
		CG	FG	WAM4	WAM4+	WAM3
S_{phil}	Cavaleri and Malanotte-Rizzoli (1981); Tolman (1992)	X	X	X	X	X
S_{in}	Komen et al. (1984)					X
	Janssen (1991)	X	X	X	X+	
S_{nl4}	Hasselmann et al. (1985)	X	X	X	X	X
S_{ds}	Komen et al. (1984)					X
	Janssen (1991)	X	X	X	X	
S_{bf}	Hasselmann et al. (1973)	X	X	X	X	X
Dissipation const. (m^2 s^{-3})		0.038	0.038	0.038	0.038	0.038
Growth limiter	Ris (1997)			X		X
	Hersbach and Janssen (1999)	X	X		X	
Propagation scheme		1st order upwind explicit			Fully implicit	
Source term integration scheme		Fully implicit			Fully implicit	
δt_p (s)		720	240		1200	
δt_s (s)		720	720		1200	
Grid size		165 × 91	286 × 121		286 × 121	
Grid resolutions						
Spatial		0.5°	0.1°		0.1°	
Spectral: Freq.		25	25		25	
Dir.		24	24		24	

X+ is the corrected SWAN implementation of WAM4
CG = coarse grid; FG = nested fine grid
δt_p is the propagation time step
δt_s is the source term integration time step

in the computation of the validation statistics. The buoy observations used in this study include wind speed, wind direction, significant wave height, and peak wave period.

Cross-comparison of the wave data from the NDBC buoy network with the data from the MSC buoy network shows discrepancies in wave height measurements between the two observing networks (J.-R. Bidlot et al., unpublished manuscript; Durant and Greenslade, 2007). It should be noted that in the cross-comparison study, wave data such as significant wave height and peak period are derived from the one-dimensional (1-d) spectra obtained by application of a Fast Fourier Transform (FFT) to the raw buoy measurements and transmitted via the Global Telecommunication System (GTS) to the meteorological community. Some factors that may have contributed to the wave height discrepancies between the two networks are now briefly described (see also AXYS Environmental Consulting Ltd., 1996; AXYS Environmental Systems, 2000; Earle, 1996). Strapdown accelerometers are installed on all MSC buoys while vertically stabilized accelerometers are installed on the NDBC and the Datawell waverider buoys on the Atlantic East Coast. Skey et al. (1998, 1999) compare the results obtained from a strapdown accelerometer with those from a Datawell vertically stabilized accelerometer and found that the former consistently underestimates wave heights by up to 10% through a wide range of sea states. The MSC and NDBC buoys sample and process wave data differently. Data acquisition start and end times, record length, sampling rate and frequency range and number of frequencies used in the summation of the 1-d spectra are different. The NDBC buoy data recording rate is 2.56 Hz while that of MSC buoy is 1.0 Hz. This gives a Nyquist frequency, f_{Nyq}, for the MSC buoys that differs from the NDBC buoys. Energies present at frequencies higher than f_{Nyq} are aliased into the frequency interval below f_{Nyq} (Bergland, 1969). In the case of the MSC buoys, MEDS recalculated H_s from the reported 1-d spectra in which the aliased energies present at frequencies below the low frequency cutoff, which is either calculated or taken to be the instrument default of typically 0.033 Hz or higher, are lost resulting in an underestimation of the MEDS H_s. However, for the NDBC buoys, energies at frequency components higher than f_{Nyq} are negligible resulting in little or no aliased energies at frequencies below f_{Nyq}. To minimize the effect of aliasing, Holthuijsen (2007, see Appendix C) suggests that for measurements at sea the wave data acquisition rate should be at least 2 Hz. FFT analyses performed on the MSC and NDBC buoy data records are segmented differently to produce the final 1-d spectra. The NDBC spectra are corrected for electronic, accelerometer and hull noise while the MSC spectra are partially corrected for electronic and accelerometer noise but no hull response corrections for the various buoys are applied in the analysis procedure. The significant wave height and peak

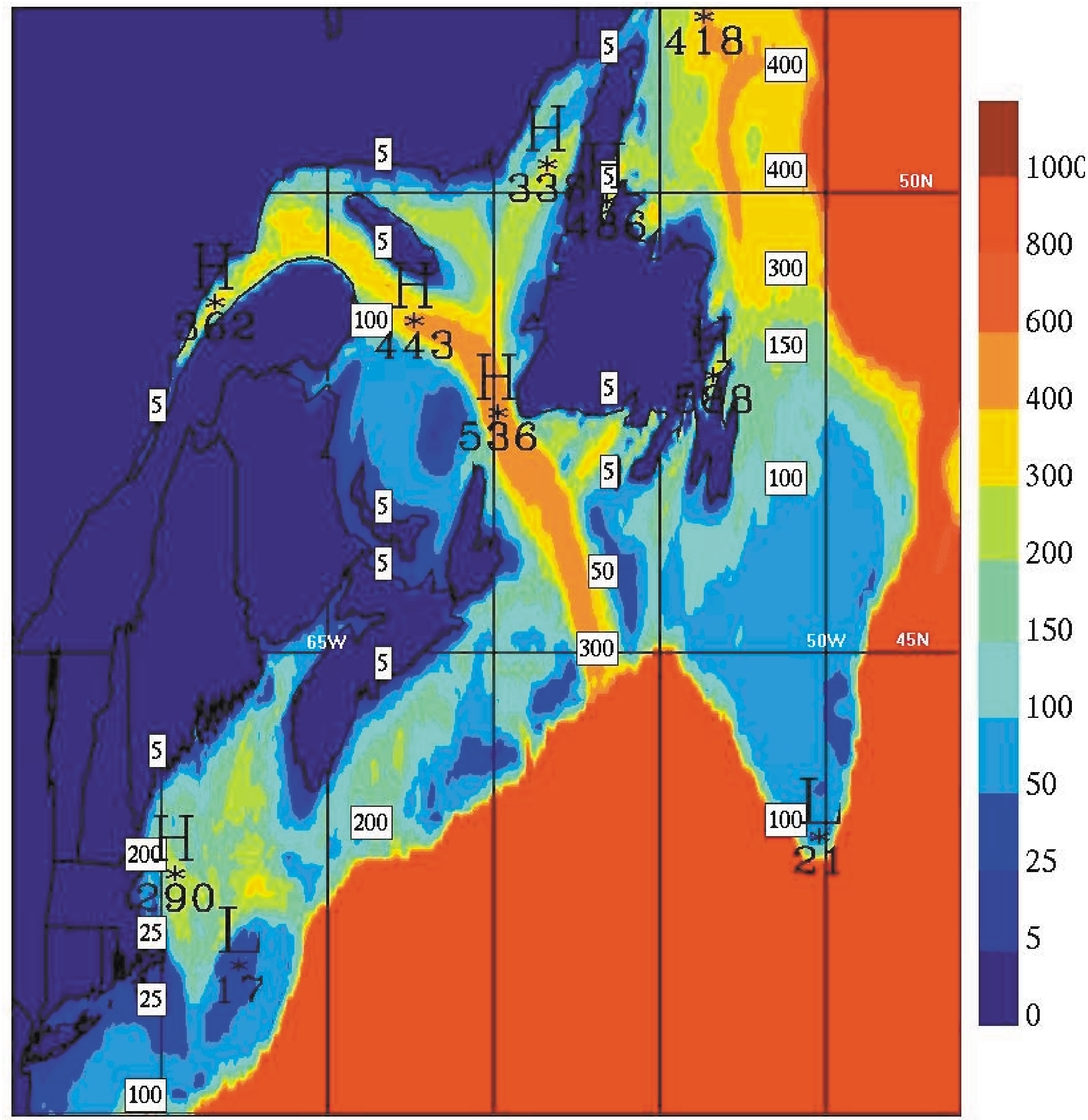

Fig. 3 Ocean bathymetry of the area covered by the nested fine grid shown in Fig. 1. The colour scale is ocean depth in metres. Depths < 5 m are set to 5 m and those > 999 m are set to 999 m.

period used in this study are those reported by the buoys. In the case of the MSC buoys, the reported values are used as opposed to the values recalculated by MEDS from the transmitted 1-d spectra derived from FFT analysis of the raw buoy data.

Table 2 also gives the peak H_s, the peak wave period T_p, and H_{max} in order of arrival times of the peak H_s as reported by the buoys and the RG3 waverider. Here, H_{max} is defined as the maximum wave height measured from crest to trough at the time of peak H_s.With the exception of nearshore buoys 44007 and 44013, the observed peak H_s ranges from 6.2 m to 12 m. The RG3 waverider, located about 37 km southwest of the western tip of Sable Island in water of depth 44 m, recorded significant wave height, peak wave period and sea level elevation data hourly at a sampling rate of 2.56 Hz. It recorded peak H_s = 12.0 m and H_{max} = 19.4 m. The extreme waves observed at RG3 were corroborated by two other Datawell waveriders in the area around the same time before they were both damaged by breaking waves. Estimates of the wave crest heights of two individual and exceptionally large waves that hit the Channel Head area of Port-aux-Basques within 10 minutes of each other were determined from observations of

TABLE 2. Buoys used in model validation statistics. The table shows the buoy names, hull IDs and water depths. Also shown are the buoy peak values of significant wave height, H_s, and the corresponding peak wave period, T_p, wave height maximum, H_{max}, and the ratio H_{max}/H_s in order of arrival times of highest waves between 21–22 January 2000. H_{max} is defined as the maximum value of the wave height measured from crest to trough at the time of peak H_s. The MEDS ID of the RG3 Datawell waverider is WEL416. All the buoys are nondirectional buoys.

WMO/ MEDS ID	Buoy name	Hull ID	Water Depth (m)	Day	Time UTC	Peak H_s (m)	T_p (s)	H_{max} (m)	H_{max}/H_s
44008	Nantucket	3D	63	21	05	8.2	10.0	–	–
44007	Portland	3D	24	21	12	1.9	6.7	–	–
44013	Boston Harbour	3D	55	21	16	3.4	9.0	–	–
45005	Gulf of Maine	6N	198	21	16	6.2	10.0	–	–
44011**	Georges Bank	6N	88	21	18	9.2	12.5	–	–
44142	Lahave Bank	6N	1300	21	18	8.7	13.5	11.8	1.36
WEL416 (RG3)+	Cohasset-Panuke	Spherical	44	21	22	12.0	13.3	19.4	1.62
44141	Laurentian Fan	6N	4500	22	03	11.6	17.1	17.6	1.52
44255	NE Burgeo Bank	6N	185	22	08	8.5	16.0	14.2	1.67
44251*	Nickerson Bank	6N	69	22	13	6.7	14.4	10.4	1.55
44140	Tail of the Bank	6N	90	22	14	7.1	17.1	11.2	1.58

3D = 3-m Discus buoy; 6N = 6-m NOMAD buoy
\+ Hull diameter = 0.9 m
* Buoy not used in validation statistics due to few observations
** Buoy stopped reporting three hours after peak H_s

the damage and water level marks (MacPhee, unpublished manuscript).

5 Results and discussion

a *Individual Peak and Extreme Wave Heights*

Figure 4 shows the complete record of sea level elevations from the RG3 waverider throughout the storm. The figure shows that the highest five waves observed at RG3 have total vertical displacements (crest to trough) greater than 19 m while two more waves reach almost 19 m. The RG3 waverider has a dynamic wave height range of –20 m to +20 m, indicating that the vertical displacements of the highest waves recorded are well within this range. The waverider sensor has a scale accuracy < 0.5% of measured value after calibration (Datawell BV, 2006). Figure 5 shows these seven extreme individual waves in the RG3 record in Fig. 4 in more detail for 12-minute duration wave records in which the zero-upcrossing H_{max} (crest to trough) of each of these waves is 19 m or more. Given that the maximum positive wave amplitude is H_+, then the calculated value of $H_{max} = 2H_+$ at the buoys by assuming that the wave shape is symmetrical. An examination of Fig. 5 indicates that H_{max}/H_+ is close to 2.0 for two of the extreme waves and <2.0 for the other five. Skey et al. (1998) points out that H_{max}/H_+ for a Datawell sensor falls below 2.0 for wave heights exceeding 8 m, confirming that in extreme sea states the wave shape is not symmetrical. The MSC buoy onboard wave processing package now returns a true crest to trough H_{max} with the changeover to this method occurring around 1998 to 1999. Since H_s is known, the ratio H_{max}/H_s is generally computed. Based on 1998 data for RG3, Borgel (2001) shows, using the frequency distribution of the ratio H_{max}/H_s for 2505 data points, that the 65th percentile has a value of 1.6, the 90th percentile a value of 1.763 and the 99th percentile a value of 2.045 for H_s > 3 m. The MSC buoys, however, have a maximum dynamic wave height range of –15 m to +15 m. The H_{max} given in Table 2 for this storm event is well within this dynamic range. However, a number of storms have occurred recently that indicate that a larger range should be considered (AXYS Environmental Consulting Ltd., 1996). The H_{max}/H_s ratios for the RG3 waverider and MSC buoys given in Table 2 range from 1.36 to 1.67 for H_s > 6 m and vary from site to site. The H_{max}/H_s values for this storm are consistent with ratios based on the RG3 1998 dataset (Borgel, 2001). The NDBC buoys, however, do not provide measurements of H_{max} data.

Port-aux-Basques reported that two extreme waves, 10 minutes apart, occurred in the Channel Head area. MacPhee (unpublished manuscript) estimated H_{max} from observations of the damage and flagstaff marks to be close to 16 m. Using the 60th percentile value of the ratio H_{max}/H_s = 1.6 based on the 1998 RG3 dataset of Borgel (2001), the corresponding H_s = 10 m which is somewhat less but comparable to the peak H_s observed at RG3.

b *Model Simulations and Wave Characteristics*

The January 2000 superstorm passed through the middle of the East Coast buoy network with buoys 44141, 44140, 44255 and RG3 located to the right, and buoys 44005, 44007, 44008, 44013 and 44142 located to the left, of the observed track as shown in Fig. 1. A comparison of the significant wave heights, H_s, obtained from the three runs of SWAN is given in Fig. 6 at four buoy locations in order to determine their relative performance when compared with each other and against observations. The SWN-WAM4 run underpredicts H_s in all cases when compared with H_s from both the SWN-WAM3 and SWN-WAM4+ runs. The results of the SWN-WAM4+ run based on the inclusion of the shift parameter z_α = 0.011 and the HJ99 wave growth limiter as given in Eq. (4) are in good agreement with those of the SWN-WAM3 run based on the WAM3 physics of Komen et

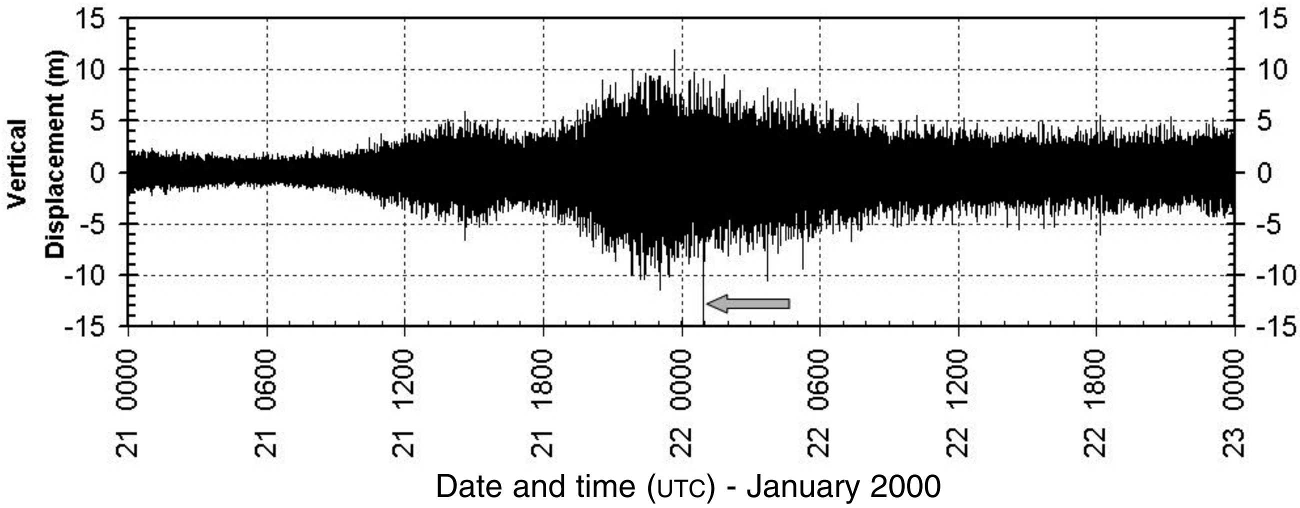

Fig. 4 Complete record of vertical displacement at RG3 as measured by the Datawell waverider at 2.56 Hz. The arrow indicates the maximum negative displacement.

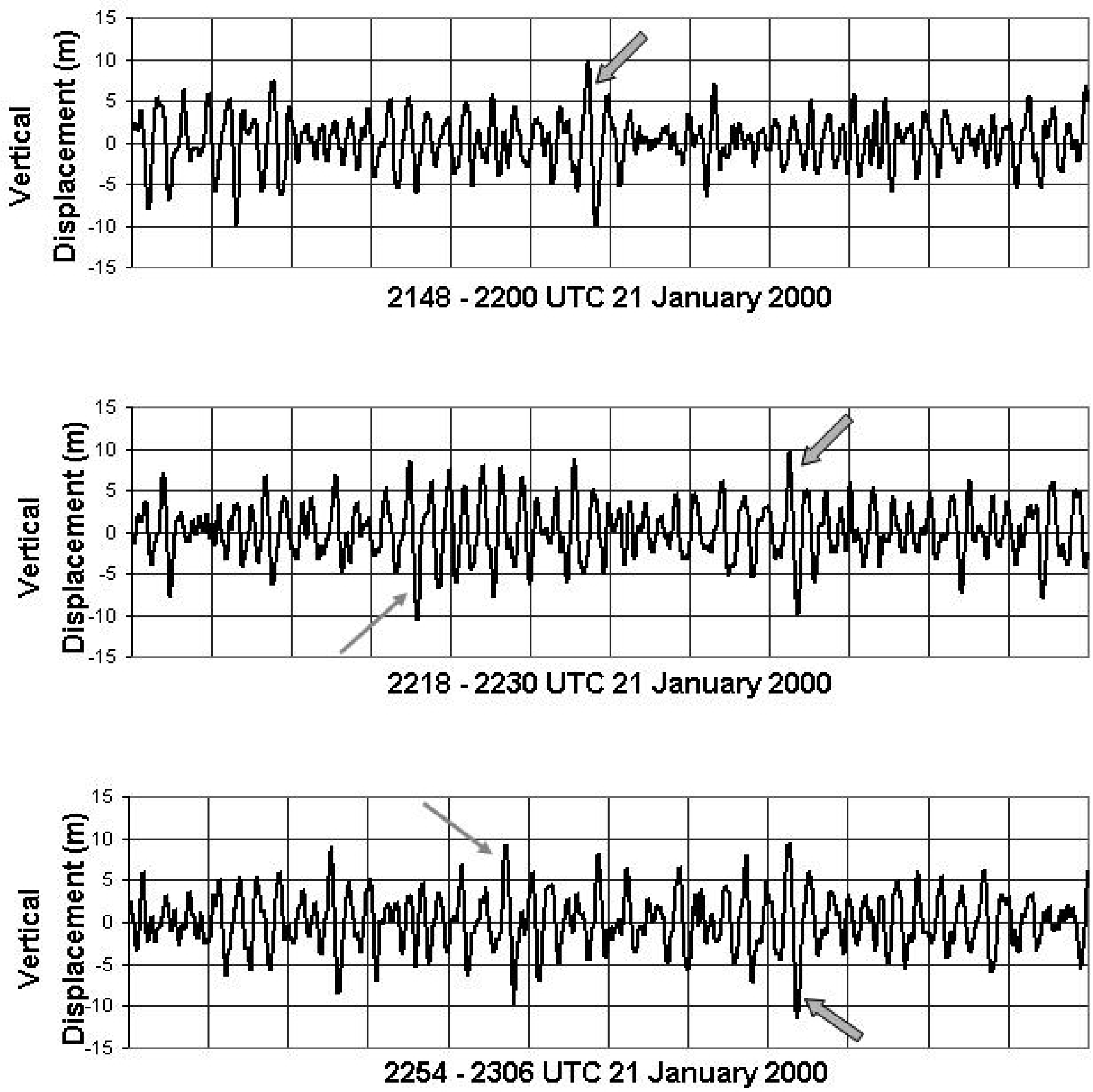

Fig. 5 Plots of 12 minute duration of the wave record in Fig. 4 showing extreme individual waves. Thick arrows mark five waves with total vertical displacement (crest to trough) of 19 m or greater. Thin arrows mark two waves with displacement of almost 19 m.

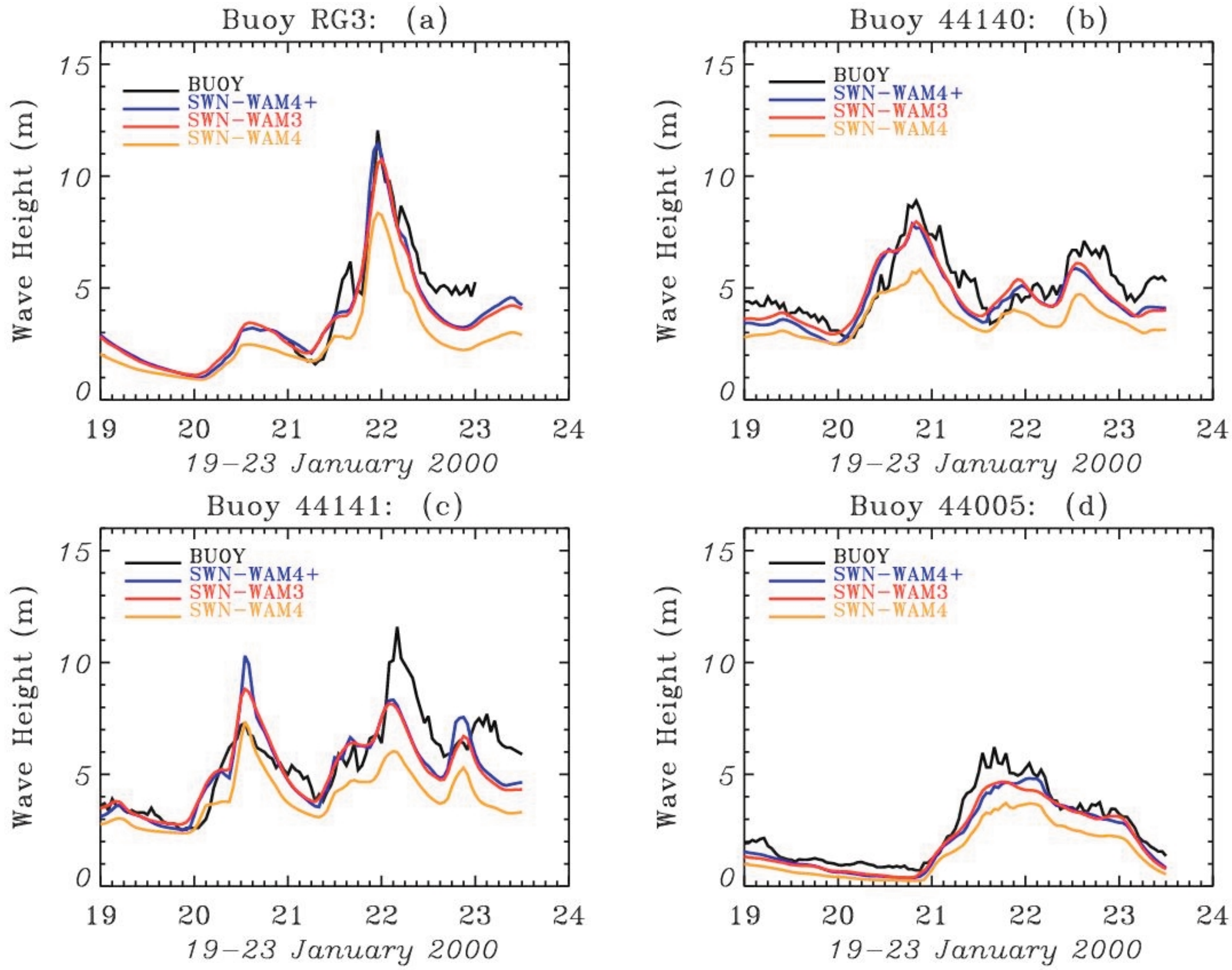

Fig. 6 Comparison of the significant wave heights, H_s, for the three SWAN runs against the buoy H_s at four locations for the period 19-23 January 2000. The black line gives the buoy H_s, the blue line the H_s based on the modified version of the SWAN implementation of Janssen's WAM4 physics denoted as SWN-WAM4+, the red line the SWAN H_s based on Komen's WAM3 physics denoted as SWN-WAM3 and the orange line the SWAN H_s based on the actual SWAN implementation of Janssen's WAM4 physics denoted as SWN-WAM4.

al. (1984) which is the default option used in SWAN. It is clear that the SWN-WAM4 H_s is always underpredicted when compared with the SWN-WAM4+ H_s. However, if SWN-WAM4+ overpredicts H_s, then SWN-WAM4 still underpredicts H_s relative to H_s from SWN-WAM4+ and may give better agreement with the buoy observations as a result of the underprediction as in the case of buoy 44141 for the peak H_s centred around 12:00 UTC 20 January. The improved H_s from SWN-WAM4+ can, therefore, be ascribed to the inclusion of z_α and the use of the HJ99 limiter since other factors such as source terms, numerical schemes, winds and grid resolutions in the two runs are identical. Similar results were also found by Lalbeharry et al. (2004). This suggests that the WAM4 physics as implemented in SWAN is in error. Since it has been established that the SWN-WAM4+ H_s is an improvement over that based on SWN-WAM4, subsequent SWAN results presented are those based on SWN-WAM4+ but for completeness and comparison, model statistics are shown for all three SWAN runs.

Model outputs are compared with buoy observations in Figs 7 to 10 at six buoys located in deep and intermediate waters. The objective here is to assess the differences, if any, between the results obtained from the SWN-WAM4+ and WAM45-FG nested fine grid runs and those from the WAM45-CG coarse grid run and between the results from the two nested versions. Figure 7 displays the significant wave height, H_s, and Fig. 8 the peak period, T_p, obtained from the WAM45-CG, WAM45-FG and SWN-WAM4+ runs. In Fig. 8 the buoy T_p is well replicated by the three model runs throughout the simulation, especially during the period of strong wave growth and decay sequences. Figure 9 gives the observed and model coarse and fine grid wind speeds which show negligibly small differences and compare well against the buoy observations. The wind speeds for the two fine grids are identical as indicated by the exact superposition of the orange and red curves as they should be. The wind speed peak around 12:00 UTC on 20 January is due to the passage of an earlier storm while that around 00:00 UTC on 22 January is

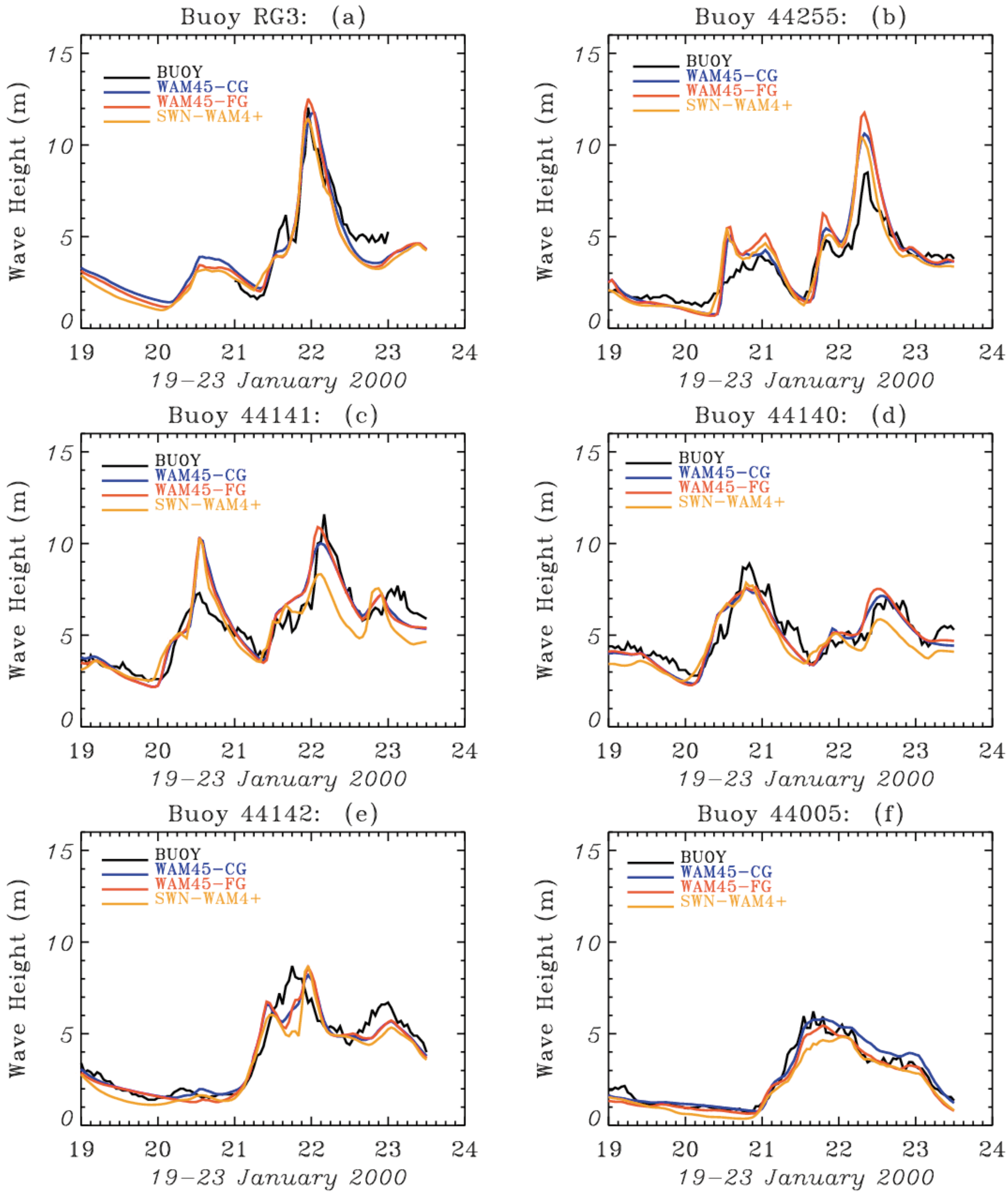

Fig. 7 Time series of observed and modelled H_s at six buoy locations for the period 19–23 January 2000. The black line gives the buoy H_s, the blue line the WAM4.5 coarse grid H_s denoted as WAM45-CG, the red line the WAM4.5 nested fine grid H_s denoted as WAM45-FG and the orange line the H_s of the modified version of the SWAN implementation of Janssen's WAM4 physics denoted as SWN-WAM4+

associated with the extreme storm which is the subject of this study. Figure 10 displays the corresponding wind directions which indicate good agreement between model and buoy measured directions.

Looking in more detail, Fig. 7 indicates that the H_s differences between WAM45-CG (blue curves) and WAM45-FG (red curves) for deep and intermediate water depths are small or minimal for the buoys on both sides of the storm track.

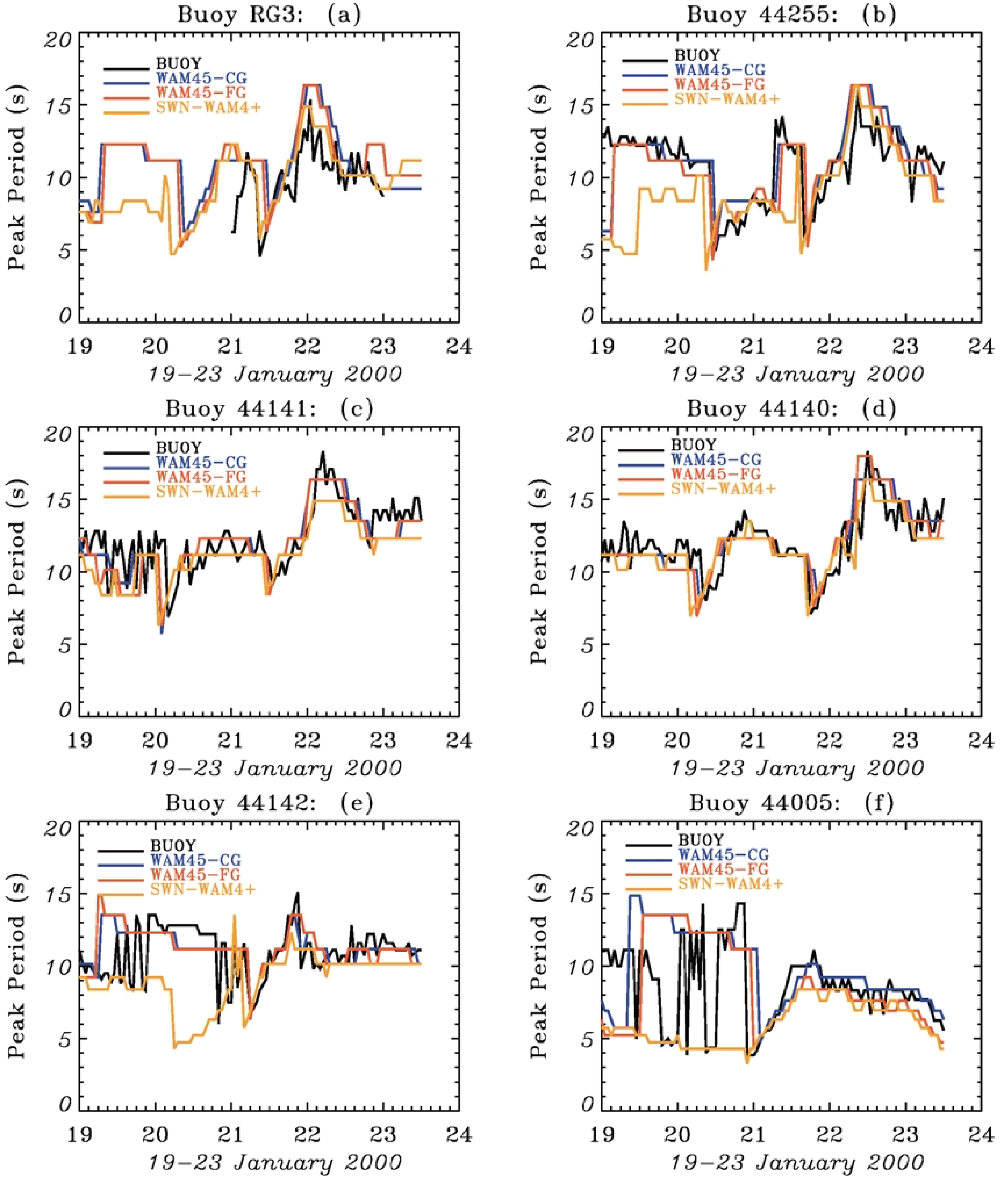

Fig. 8 As in Fig. 7 but for peak wave periods.

This suggests that for open water applications the coarse resolution WAM4.5 adequately simulates the extreme waves associated with this storm event and that a high resolution WAM4.5 may not be necessary except for nearshore applications. Another caveat is that small islands and shallow submerged bathymetric features may be unresolved by the coarse grid resolution and this may have an effect on the coarse grid model results, for example, unresolved small islands will not produce the necessary wave propagation blocking (Janssen et al., 2005). Comparison of the peak H_s of SWN-WAM4+ (orange curves) with that of WAM45-FG (red curves) shows reasonably good agreement for some of the peaks. At buoy locations where the agreement is good, the wave climate is locally wind-sea dominated and where the agreement is not as

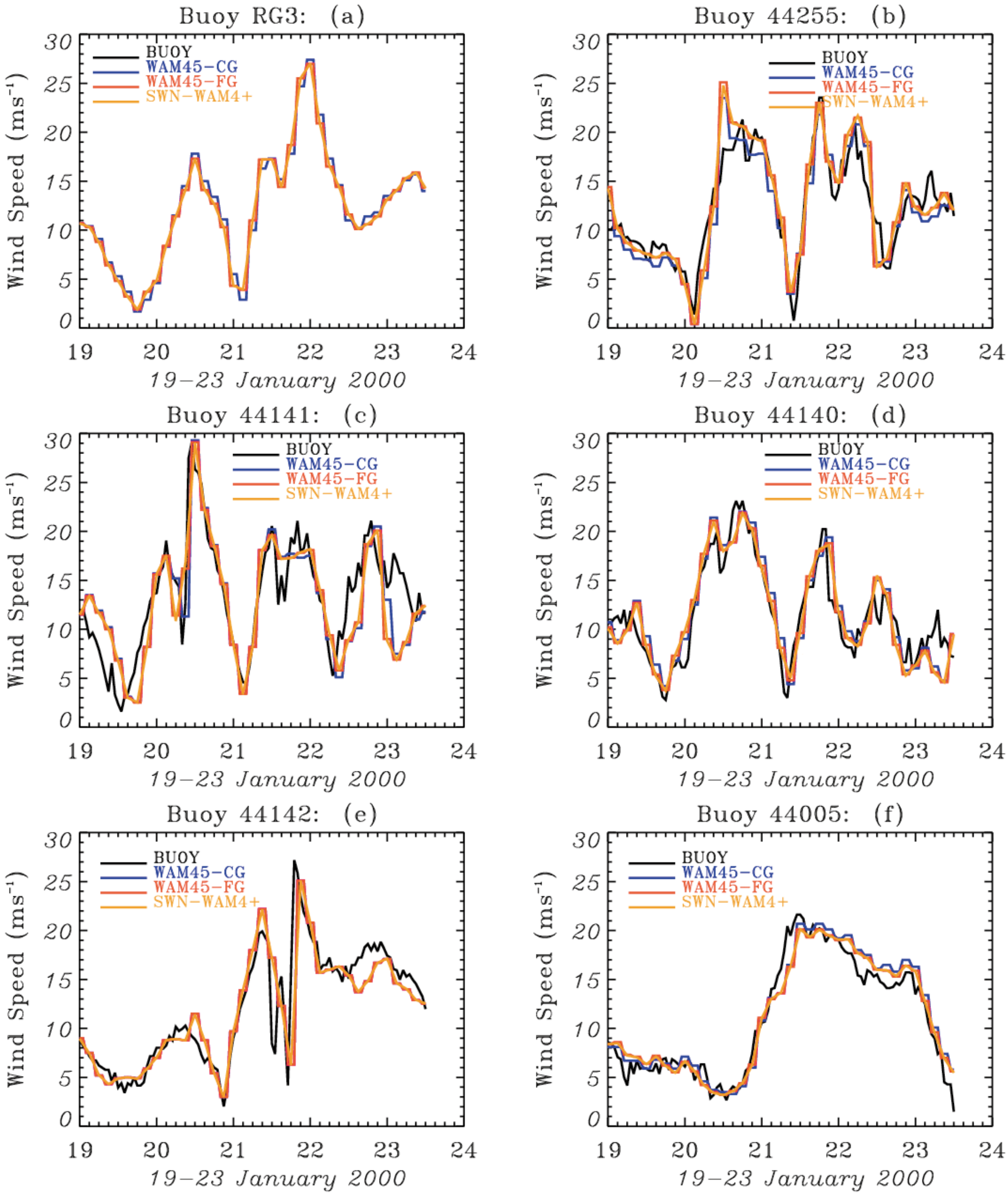

Fig. 9 As in Fig. 7 but for the 10 m level wind speeds. The black line gives the buoy wind speed, the blue line the WAM4.5 coarse grid wind speed denoted as WAM45-CG, the red line the WAM4.5 nested fine grid wind speed denoted as WAM45-FG and the orange line the SWAN wind speed denoted as SWN-WAM4+. Note that the observed wind speeds at buoy RG3 are not available.

good, for example, the second peak in Fig. 7c and in Fig. 7d, respectively, and to a lesser extent the major peak in Fig. 7e, the local wave climate is swell dominated. This disagreement may be due to the propagation scheme used by SWAN in non-stationary mode in which the so-called garden-sprinkler effect may show up for propagation over large distances and to the difference in the swell separation methods used by SWAN and WAM4.5.

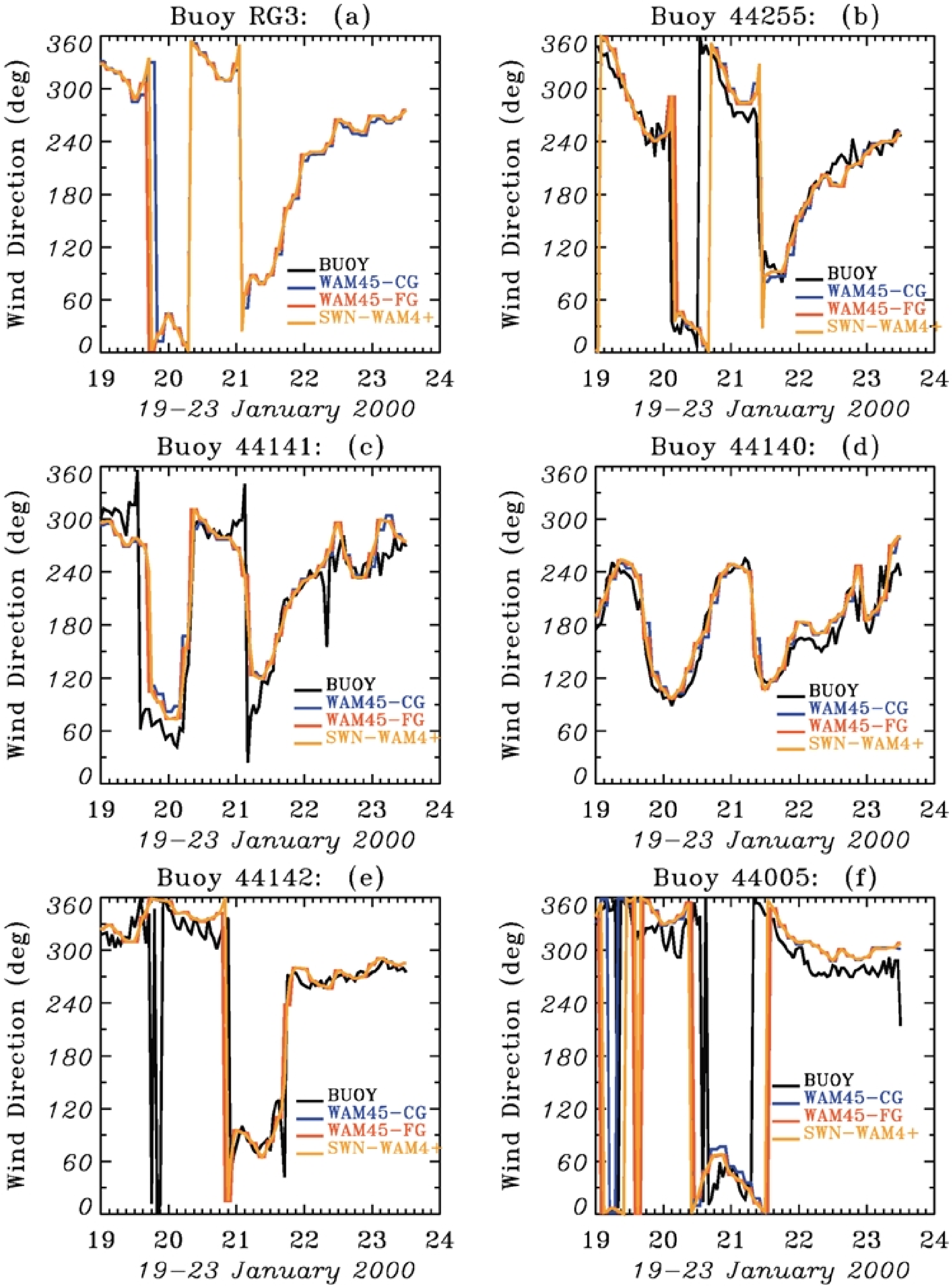

Fig. 10 As in Fig. 9 but for wind direction. Note that the observed wind direction at buoy RG3 is not available.

The RG3 waverider, located just to the right of the storm track, reported a peak H_s of 12 m around 00:00 UTC on 22 January as shown in Fig. 7a. The three model runs are in excellent agreement with the observed peak H_s both in terms of intensity and arrival time. The wave growth and decay phases are replicated well by the three runs using WAM4+ physics in the SWAN run as well as in the two WAM4.5 runs. The same is also true for the peak period T_p shown in Fig. 8a, especially during the growth phase of the peak H_s. The deep water peak wavelength based on the observed peak period T_p = 15 s given in Fig. 8a is $L_p = 1.56T_p^{\,2} = 350$ m. Since RG3 is located in water of depth h = 44 m, the ratio $h/L_p = 0.13$, which implies that the waves at RG3 effectively 'feel bottom' as they transition from deep to shallow waters since for transitional water depth $0.04 < h/L_p < 0.25$ (WMO, 1998). This is consistent with the wave scouring action on the sea floor as indicated by settling of the legs of rigs operating near Sable Island (Borgel, 2001).

Buoy 44255 in Fig. 7b is located to the right of the storm track and to the northeast of RG3. It is about 40 km off the southwest coast of Newfoundland (see Fig. 1) in water of depth 185 m in a minor submarine ridge that runs southwest to northeast shown in Fig. 3. It measured a peak H_s of 8.5 m around 09:00 UTC on 22 January. Both the SWAN and WAM4.5 overpredict the peak H_s by 1.5 m to 3.0 m but give its time of occurrence accurately. The model wave growth is slightly higher than the observed wave growth but the decay sequence is well replicated by the three model simulations. This overprediction cannot be ascribed to wind speed overprediction since the model and observed wind speeds are in good agreement as seen in Fig. 9b. The peak winds occur around 05:00 UTC on 22 January but the waves continue to increase in height and peak period (see Fig. 8b) for another four hours. Based on the model outputs of H_s, swell wave heights (hereinafter denoted as H_{swl}) and winds between 00:00 UTC and 09:00 UTC on 22 January, the sea is locally wind-sea dominated. Distant swells range from 0.9 m to 2.0 m and model H_s from 5.0 m to 12.0 m with swells becoming more dominant some three hours later around 12:00 UTC on 22 January. The wind direction is south-southeast at 00:00 UTC becoming southerly by 09:00 UTC. Since the swells are not the dominant factor, errors in the far-field winds are unlikely to contribute to this overprediction. A more plausible explanation is that this overprediction may be due to the role of the model dynamic fetch as discussed in Section 5c.

Buoys 44141 and 44140 lie well to the right of the observed storm track. The peak H_s observed by buoy 44141 in Fig. 7c at 12:00 UTC and that by buoy 44140 in Fig. 7d at 21:00 UTC on 20 January, respectively, are both due to the passage of an earlier storm. In both cases the SWAN run and the two WAM4.5 runs are in very good agreement with each other. In the case of buoy 44141, the models overpredict the peak H_s by 3 m while in the case of buoy 44140, there is a slight underprediction of about 1 m but the arrival times of the two peaks are well replicated. The question, therefore, arises as to why there is gross overprediction by all three model runs in one case and reasonably good agreement in the other, considering the fact that the wind speeds are in good agreement with the observed winds speeds shown in Figs 8c to 8d and that the waves are wind-sea dominated at both buoy locations, that is, the peaks are not affected by distant swells. During the period 09:00–18:00 UTC on 20 January buoy 44141 lies behind a sharp north-south wind trough which moves somewhat slowly eastward. Wind directions are primarily west-northwest and fetch conditions remain unchanged. From 09:00–12:00 UTC the model wind speed increases very rapidly from 15 m s^{-1} to 29 m s^{-1} while for the same period the model waves grow from $H_s = 5$ m to a peak $H_s = 10$ m. At the start of the period of rapid wave growth, the sea is swell dominated with $H_{swl} = H_s = 5$ m and becomes wind-sea dominated towards the end of the period with a model wind-sea wave height (hereinafter denoted as H_{wse}) of 9.4 m given that the swells arriving at buoy 44141 from the south-southeast have a wave height of 3.5 m. The model T_p remains unchanged at 11 s giving a deep water $L_p = 188$ m, a local wave steepness $H_s/L_p = 0.050$ and $H_{lim} = K{*}L_p = 9.2$ m which is close to the model peak $H_s = 10$ m. The three-hour average wind speed is 22 m s^{-1} giving a Pierson and Moskowitz (1964) equilibrium wave height $H_{PM} = 11.8$ m for a fully developed sea state. The wind-sea wave height, H_{wse}, grows from 0 m to 9.4 m during the three-hour period as the wind speed increases from 15 m s^{-1} to 29 m s^{-1}. This very rapid growth of H_{wse} suggests that the wind input, S_{in}, dominates the whitecapping dissipation, S_{ds}. Since the waves are not fully developed and bottom friction plays no role as the waves are deep waver waves, the model wind-sea waves continue to grow until the local wave steepness reaches a value close to the limiting value $K = 0.049$ before breaking, resulting in the SWAN and the two WAM4.5 runs overpredicting the buoy peak $H_s = 7$ m by 3 m.

At buoy 44140 the observed peak H_s occurs at 18:00 UTC on 20 January. The three model runs are in good agreement with each other. They underpredict the peak H_s by 1.0 m but correctly give its arrival time. During the three hours before the peak H_s is reached, the wind speed increases from 19 m s^{-1} to 22 m s^{-1} while the model H_s increases from 7.0 m to 8.0 m. During the following three hours the wind speed decreases from 22 m s^{-1} to 20 m s^{-1} and the model H_s from 8 m to 7 m. The wind direction during this six-hour period changes from south-southeast to south-southwest giving a relatively small change in the fetch. The wind speed and wave growth and decay sequences are more gradual in this case and allow for better agreement between model and observation since the wave height growth rate and its dissipation rate are nearly the same. The observed T_p in Fig. 8d is 14 s giving a deep water $L_p = 306$ m and the ratio $h/L_p = 0.29$ where $h =$ 90 m is the water depth at buoy 44140, that is, the waves are still deep water waves and hence bottom friction does not contribute to the wave dissipation.

The second peak H_s in Fig. 7c and in Fig. 7d is generated by the storm under current study. The waves arriving at these buoys are mainly swells coming from the generating area left behind by the storm moving rapidly northward. The somewhat poor performance of the SWN-WAM4+ run in the swell-dominated areas has already been explained while the two WAM4.5 runs replicate the observed peak H_s and the arrival times at both locations reasonably well. At 03:00 UTC on 22 January the WAM45-FG run gives, at buoy 44141, a peak $H_s = 10.8$ m, a peak $H_{swl} = 9.9$ m and a $T_p = 16$ s while at 12:00 UTC on 22 January at buoy 44140, the peak $H_s = 6.6$ m, $H_{swl} = 6.5$ m and $T_p = 18$ s. Since the local sea is swell dominated at both locations, the swell peak period is the same as T_p. The deep water swells leaving buoy 44141 travel northeastward towards buoy 44140, a separation distance of approximately 450 km. With a group speed of 14 m s^{-1}, the travel time taken by the swells to reach buoy 44140 is close to nine hours, which agrees reasonably well with the difference in arrival times of the peak H_{swl} at the two buoys. The swells depart from buoy 44141 with a peak H_{swl} = 9.9 m and arrive at buoy 44140 with a peak H_{swl} = 6.5 m, a reduction of 3.4 m in the peak H_{swl}. The so-called garden sprinkler effect is small or negligible for the separation distance of 450 km between the two buoys. With a swell T_p = 18 s at buoy 44140, the deep water peak swell L_p = 505 m and h/L_p = 0.18 for buoy 44140. In the transition from deep to shallow waters the swells approaching buoy 44140 from buoy 44141 suffer a reduction in swell wave height of approximately 3.4 m resulting from loss of wave energy due to the bottom friction source term S_{bf}.

The model outputs for buoy 44142, which lies just to the left of the storm track, are presented in Figs 7e, 8e, 9e and 10e and for buoy 44005, also to the left of the track but about 100 km from the coast in water of depth 200 m, in Figs 7f, 8f, 9f and 10f, respectively. In Fig. 7e the observed peak H_s = 8.7 m occurs at 18:00 UTC on 21 January while the model peak H_s of 6.7 m occurs at 10:00 UTC and the model peak of 8.6 m at 23:00 UTC on 21 January, respectively, are in response to the model wind speed peaks in Fig. 9e around the same times. All models reflect a decrease in energy levels following the trend in the local winds between 15:00 UTC and 18:00 UTC on 21 January. During this period the storm centre passes just to the right of buoy 44142 which recorded a minimum pressure of 948 hPa and a minimum wind speed of 4 m s^{-1} at 17:00 UTC. The sea at this time is highly swell dominated with the model swells arriving at buoy 44142 from the south-southwest sector which is also corroborated by the increase in T_p from 11 s to 14 s shown in Fig. 8e. The observed H_s is higher than the model H_s during a period of minimum model and observed wind speeds suggesting that the observed H_s consists mostly of swell components that are somewhat stronger than the model H_{swl} which leads to a higher observed H_s at 15:00 UTC. As the observed wind speed increases from a low of 4 m s^{-1} to 26 m s^{-1} by 19:00 UTC as shown in Fig. 9e, the observed peak H_s reaches a value of 8.7 m at 18:00 UTC. Examination of Fig. 9e indicates that the buoy peak wind speed of 26 m s^{-1} at around 19:00 UTC decreases to 22 m s^{-1} during the following two hours while the model wind speed peak of 25 m s^{-1} which occurs about one to two hours later remains unchanged for the next two hours. This time lag of one to two hours by the model peak wind speed results in a phase error between the buoy and model peak H_s.

At buoy 44005 in Fig. 7f the peak H_s of 6 m is observed at 18:00 UTC on 21 January. The two WAM4.5 runs are in excellent agreement with each other and replicate the buoy observations well. The SWN-WAM4+ run underpredicts the peak H_s by 1.0 m, otherwise the agreement with measurements is also quite good. Figure 9f indicates that the coarse and fine grid winds are identical and agree well with the buoy winds. During the period of wave growth from 09:00–18:00 UTC, the winds are mainly from the northwest with a wind speed near 20 m s^{-1}. Fetch and wind conditions remain almost unchanged during the growth phase of the peak H_s as the storm moves northwards. The resulting sea is mainly wind-sea dominated in which both the model T_p and the observed T_p reach a typical wind-sea value close to 10 s.

Two exceptionally large individual waves struck the Channel Head area of Port-aux-Basques. The first wave arrived at approximately 06:30 UTC on 22 January followed by a second wave about 10 minutes later. The maximum wave height determined from observations of the damage and flagstaff marks was estimated to be about 17 m (MacPhee, unpublished manuscript) and the tide about 0.7 m above the Lowest Low Water (LLW) datum line, respectively. The storm surge might have contributed about 0.8 m to the sea level as mentioned earlier (Bobanovich et al., 2006) so that the corrected H_{max} was closer to 16 m. Assuming that this value is reasonably accurate, then using the 65th percentile value of the ratio H_{max}/H_s = 1.6 based on the 1998 RG3 dataset (Borgel, 2001), H_s is calculated to be about 10 m. As shown later, the wave model output indicates that at 06:00 UTC on 22 January there is a wave height contour near 12 m about 30 km south of the Channel Head area in Cabot Strait in the Laurentian Channel. The model waves move northward with a peak period of 15 s and a deep water group velocity of 11.5 m s^{-1} reaching the Channel Head area in about 30 minutes, that is, at 06:30 UTC on 22 January, the time the first exceptionally large wave was observed. Although the model 10 m wave height contour arrives somewhat earlier than the 12 m contour in the Channel Head area, the simulation of such extreme wave height by the wave model lends credence to the possibility of occurrence of the two so-called ‘freak’ waves that were generated by this storm.

c *Observed and Model Dynamic Fetch*

Dynamic or trapped fetch occurs when the generating area of the storm waves moves with the waves it generates (Bigio, 1996). For deep water waves the group velocity is $c_g = gT/(4\pi)$. In resonance, the waves move with the same speed and in the same direction as the storm or the fetch area. In other words, the storm speed $V_s = c_g = gT_{res}/(4\pi)$ where T_{res} is the resonant period. When resonance occurs, fetch and duration are effectively unlimited (unless the fetch changes speed or direction or the waves reach a coast) and all waves will amplify. But the waves with the greatest amplification will be those whose period is equal to T_{res} which may or may not be equal to T_p. Given V_s, T_{res} is determined and H_{lim} is obtained from Eq. (6) with T_{res} replacing T_p. In storm situations, if the peak period $T_p = T_{res}$ then the dominant waves will become more extreme and may reach H_{lim}. However, even in dynamic fetch situations the H_s steepness value will not exceed the steepness limit K = 0.049. Although dynamic fetch theory is more applicable to small storm systems such as tropical cyclones or hurricanes, its occurrence in large extratropical storm systems is not uncommon. Dynamic fetch in relation to tropical cyclones is discussed in Bowyer and MacAfee (2005) and MacAfee and Bowyer (2005).

Now consider the buoy and model waves at buoy 44255 at 09:00 UTC on 22 January in Fig. 7b. Between 18:00 UTC on 21

January and 06:00 UTC on 22 January, the storm moves northward (see Fig. 1) with an observed average speed V_{obs} = 15.5 m s^{-1} which gives a resonant T_{res} = 20 s. The observed T_p = 16 s and the corresponding deep water c_g = 12.5 m s^{-1} at 09:00 UTC. Since there is a large difference between c_g and V_{obs} as determined from the observations, we conclude that in the observation space dynamic or trapped fetch plays no role in enhanced wave growth in this storm. However, a small difference may exist between the model c_g and V_{mod} which can give rise to a trapped fetch condition in the model as discussed in the next paragraph.

The motion of the model wind system associated with the model storm surface pressure system as given by the weather prediction model gives a good approximation of the model storm motion, which may or may not be the same as the observed storm motion. Since the model wave system is generated by the model wind system, it is reasonable to conclude that if the motion of the wind system and the motion of the dominant wave system are nearly the same and in the same direction, this dominant wave system will be seen as being trapped in the model space and would provide a plausible explanation of the model overprediction of the peak wave height. This idea is used here to help explain why the model peak waves are overestimated at buoy 44255. In this case the model storm also moves mainly northward (see Fig. 1) but with a slight northwestward component with an average northward speed V_{mod} = 14 m s^{-1} and a corresponding T_{res} = 18 s. Figure 11 displays the model results for the WAM45-FG run for three hindcast hours since there are minimal differences between this run and the WAM45-CG run. The figure shows snapshots of the modelled wave and wind systems and the corresponding peak periods for three specific hours, namely, 18:00 UTC on 21 January, 00:00 UTC and 06:00 UTC on 22 January. An examination of Figs 11a to 11c indicates that the model shows an area enclosed by the 12 m contour moving northward towards the Channel Head area. The corresponding peak period increases from 14 s at 18:00 UTC on 21 January (Fig. 11f) to 16 s at 06:00 UTC on 22 January (Fig. 11d) just south of buoy 44255 in the Laurentian Channel. This gives a deep water model c_g = 12.5 m s^{-1} at 06:00 UTC. In this case the small difference between c_g and V_{mod} suggests that in the model space dynamic or trapped fetch may have contributed somewhat to enhanced wave growth. As shown in Fig. 9b the model wind speeds are in good agreement with the buoy measured wind speeds so that the overestimation of the peak H_s cannot be ascribed to wind speed overestimation. Distant swells are not a dominant factor since the swells arrive some three hours later so that errors in the far-field winds are not likely to contribute to this overprediction. We, therefore, conclude that the model dynamic fetch is the most likely mechanism responsible for the overprediction of the model peak H_s of 11.5 m around 09:00 UTC on 22 January at buoy 44255. Also, for T_{res} = 18 s (based on the model storm track speed of 14 m s^{-1}), the corresponding H_{lim} = 25 m, so that although the model value of 11.5 m is an overprediction, it is well below the parametric boundary established by Eq. (6).

d *Validation Statistics*

The buoy data provide an independent data set to evaluate the accuracy or quality of the model wave parameters objectively. Table 3 presents the validation statistics for the significant wave heights for the five model runs based on collocations of time-paired model and buoy values for the period 00:00 UTC on 19 January to 12:00 UTC on 23 January. The collocated data set consists of the buoys listed in Table 2, except buoy 44251 which is specifically excluded because of too many data gaps. The mathematical definitions of the statistics used in this study are given in the Appendix. By definition, a positive bias denotes overprediction and a negative bias underprediction by the model. In the computations of the anomaly correlation, *ac*, and the reduction of variance, *rv*, the buoy mean of all the observations is used as climatology. The parameters *ac* and *rv* are skill scores since they provide a measure of the accuracy of the model wave parameter relative to the accuracy of a climatological forecast. The model value is considered to be useful if *ac* exceeds the threshold value of 0.6 or 60% (Janssen et al., 1997) and better than climatology for $rv > 0.0$.

An examination of the statistics for the three SWAN runs indicates that the SWN-WAM4+ statistics are better than those of SWN-WAM4 and in closer agreement with those of SWN-WAM3. This suggests that the modifications to the SWAN implementation of the WAM4 physics are preferable. More testing and validation may be required in order for the WAM4 physics to replace the WAM3 physics in SWAN as the default option. In the case of WAM4.5 the differences between the WAM45-CG and WAM45-FG statistics are minimal. In other words, in deep and intermediate water depths the performance of the coarse grid WAM4.5 is quite comparable with that of the nested fine grid WAM4.5. The statistical results confirm the earlier conclusions in Section 5b related to the use of a regional coarse grid WAM4.5 to produce operational wave forecasts in the areas of interest to Canadian wave forecasting centres. A comparison of the WAM45-FG and SWN-WAM4+ statistics reveals that the statistics are quite comparable and that differences are negligibly small. This is encouraging in that the same physics in two different models should produce results that are consistent and in close agreement. Examination of the WAM45-CG, WAM45-FG and the SWN-WAM4+ statistics indicates that the biases are relatively small, especially in the case of WAM4.5. The models show skill in the sense that $ac > 60\%$ and all the *rv* are positive, that is, the model wave heights generated are better than climatology. The scatter index, SI, which measures the accuracy normalized by the mean of the observed variable, ranges from 23 to 27%. The objective of ocean wave modellers is to achieve an SI of the order of 15% or less. Nevertheless, an SI of 23% for such an extreme storm case is considered acceptable (Jensen et al., 2006; Cardone et al., 1995).

Figure 12 presents scatter plots of model versus buoy wave heights for the period 19–23 January 2000. The solid black lines denote a perfect fit to model and observed values and the

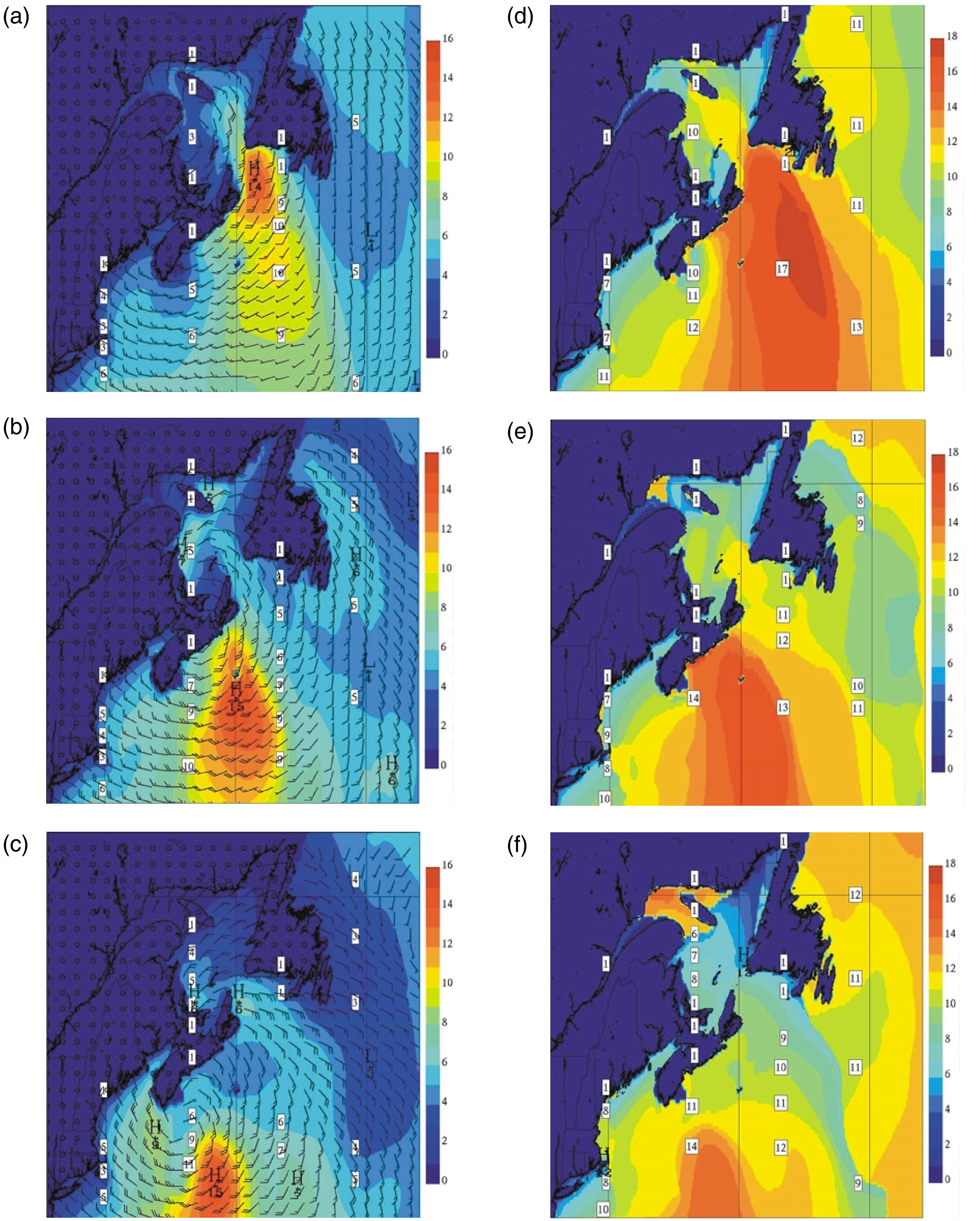

Fig. 11 Snapshots of WAM4.5 nested fine grid H_s (m) and 10 m level winds (m s^{-1}) in (a) – (c) and peak periods (s) in (d) – (f). Bottom panels are valid at 18:00 UTC 21 January, middle panels at 00:00 UTC 22 January and top panels at 06:00 UTC 22 January 2000, respectively. Winds are given in meteorological convention. Full wind barb is 10 m s^{-1} and half wind barb 5 m s^{-1}.

TABLE 3. Wave height validation statistics based on the buoys in Table 2 for the period 19–23 January 2000 for the five different model runs. See the Appendix for definitions of statistical parameters.

	WAVE HEIGHT STATISTICS (m)				
	WAM45-CG	WAM45-FG	SWN-WAM4	SWN-WAM4+	SWN-WAM3
Buoy mean	3.408	3.408	3.408	3.408	3.408
Model mean	3.497	3.379	2.352	3.100	3.102
Bias	0.090	–0.029	–1.056	–0.308	–0.306
Rmse	0.802	0.799	1.462	0.914	0.888
SI	0.235	0.234	0.429	0.268	0.261
r	0.939	0.941	0.928	0.926	0.932
ac	0.939	0.942	0.772	0.918	0.922
rv	0.877	0.878	0.591	0.840	0.849
a	0.328	0.099	0.170	0.169	0.235
b	0.930	0.963	0.640	0.860	0.841
N (no. of obs.)	990	990	990	990	990

dashed lines the best fit linear regression lines with slopes *b* and y-intercepts *a* as given in Table 3. The plots complement the statistics in Table 3 and they provide a more appealing way of displaying the same information. Wave heights in excess of approximately 5 m are better predicted by both the WAM45-CG and WAM45-FG shown in Fig. 12a and Fig. 12b, respectively, while the SWN-WAM+ and SWN-WAM3 give somewhat more spread as confirmed by the regression lines in Fig. 12d and Fig. 12e, respectively. The SWN-WAM4 in Fig. 12c consistently underpredicts the wave heights, hence the large negative bias and rmse in Table 3. For a given buoy wave height, the regression lines for the two WAM4.5 runs give a better estimate of the corresponding model wave height than the regression lines for the three SWAN runs. It is obvious also that the SWN-WAM4 regression line gives a much lower estimate of the model wave height than the SWN-WAM4+ regression line.

6 Storm waves compared with climatology

The joint frequency distribution plots in Fig. 13 present the wave climate for buoys 44141 and 44142 based on the hourly records of H_s and T_p for approximately the 14-year period from September 1990, when the buoys were first deployed, to 18 January 2005. Superimposed upon each plot is Buckley's (1988) empirical wave steepness curve which shows a well-defined envelope of extreme combinations of H_s peaks and their corresponding T_p limited by wave steepness corresponding to about 1:20.5. Also plotted is the wave height limit for steepness 1:15 which shows that this steepness is rarely exceeded. The right-hand side of the envelope, although less well defined, shows the extent of highest significant wave heights with the longest wave periods. These would most likely be fully developed seas resulting from wave generating areas in intense storms with extremely long fetch and/or duration. The storms may cover large areas or move at speeds resonant with the group velocities of the dominant waves to create dynamic or trapped fetches so that the strongest winds remain with the waves as they travel to generate enhanced wave growth. The peak values from the January 2000 storm lie on the upper portion of the right-hand side of this envelope.

At buoy 44141 in Fig. 13a the location of the January 2000 storm in the wave climate lies at the intersection of the observed H_s peak of 11.6 m and the corresponding T_p of 17.1 s with the maximum T_p of 18.3 s being reached an hour later (see Fig. 8c). It can be seen also in Fig. 13a that only about 14 storms in the climate record of buoy 44141 have peak periods of more than 17 s with corresponding H_s peaks of 11 m or more. These storms include hurricanes Luis (1995), Danielle (1998) and Gert (1999). The longest T_p of 19.7 s with a corresponding H_s peak of 10 m is produced by the 15 March 1993 storm. The January 2000 storm, therefore, is particularly rare because of such long wave periods occurring with significant wave heights of 11 m or more.

At buoy 44142 in Fig. 13b the H_s peak and the maximum T_p do not occur simultaneously during the January 2000 storm as seen in Fig. 7e and Fig. 8e. The observed H_s peak is 8.7 m with a corresponding T_p of 13.5 s at 18:00 UTC on 21 January. The maximum T_p is 15.1 s with a corresponding H_s peak of 8.0 m occurring three hours later. It can be seen in Fig. 13b that only a small number of storm waves exceeds 8.0 m with peak periods > 13.5 s and that only five storms generate H_s > 8.7 m with T_p = 15.1 s. The H_s peak of 11.2 m and the corresponding T_p of 15.1 s were produced by hurricane Juan at 00:00 UTC on 29 September 2003 and the H_s of 12.7 m and T_p of 15.1 s by the superbomb of 14 January 2002.

7 Summary and conclusions

The summary results presented here are for a specific storm case and, therefore, may not be generalized to larger samples, or even other storms. In this study two state-of-the-art third generation ocean wave models, namely the WAM4.5 and SWAN, are utilized in numerical wave simulations of the extreme storm of 19–23 January 2000 over the northwest Atlantic. This storm produced destructive waves that struck the Port-aux-Basques area in southwestern Newfoundland and other communities on the south coast of Newfoundland and the eastern shores of Nova Scotia with a high storm surge recorded in Charlottetown, PEI. WAM4.5 runs on a coarse grid while SWAN and a nested version of WAM4.5 run on a fine grid using the boundary conditions provided by the coarse grid WAM4.5. The two models described in Section 2

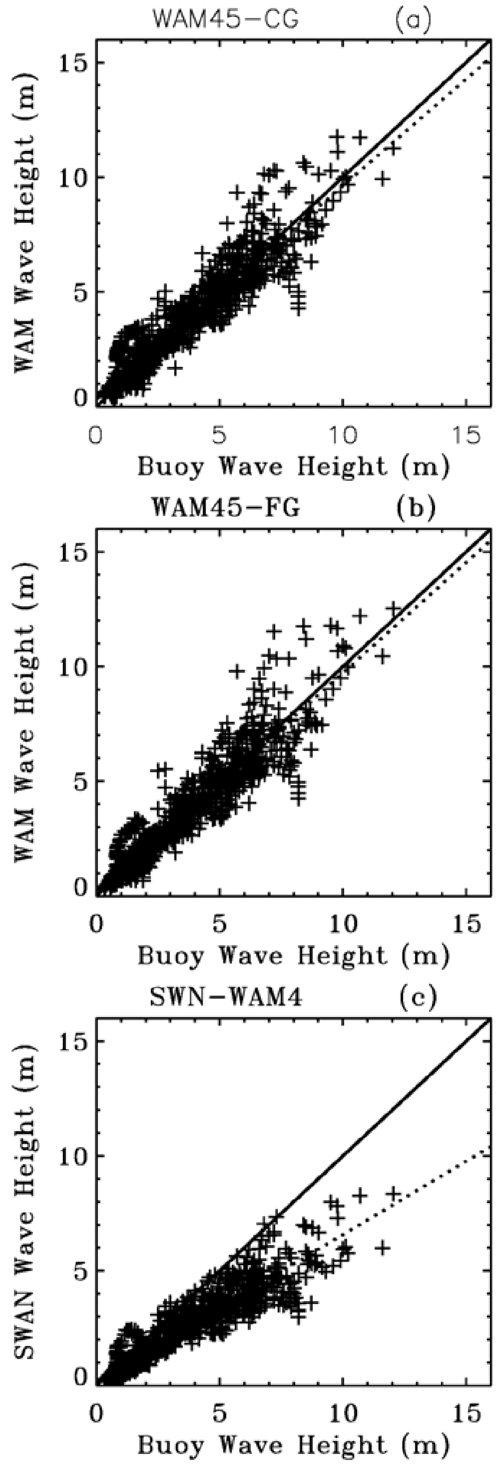

Fig. 12 Scatter plots of model versus observed significant wave heights for the period 19–23 January 2000. The plots are for the five model runs as defined in the text.

use shallow water physics, time-independent water depths and no currents and are forced by winds provided by the CMC regional GEM model at three-hour intervals. SWAN uses the WAM3 rather than the WAM4 physics of S_{in} and S_{ds} as the default option because the WAM4 physics, as implemented in SWAN, produces model results that are somewhat poorer than the WAM3 physics when compared with observations. The SWAN implementation of WAM4 is modified to include the shift growth parameter in the wind input source term S_{in} and the Hersbach-Janssen wave growth limiter and this modified version of WAM4 is used as another SWAN option. The model outputs of wave heights, peak periods and

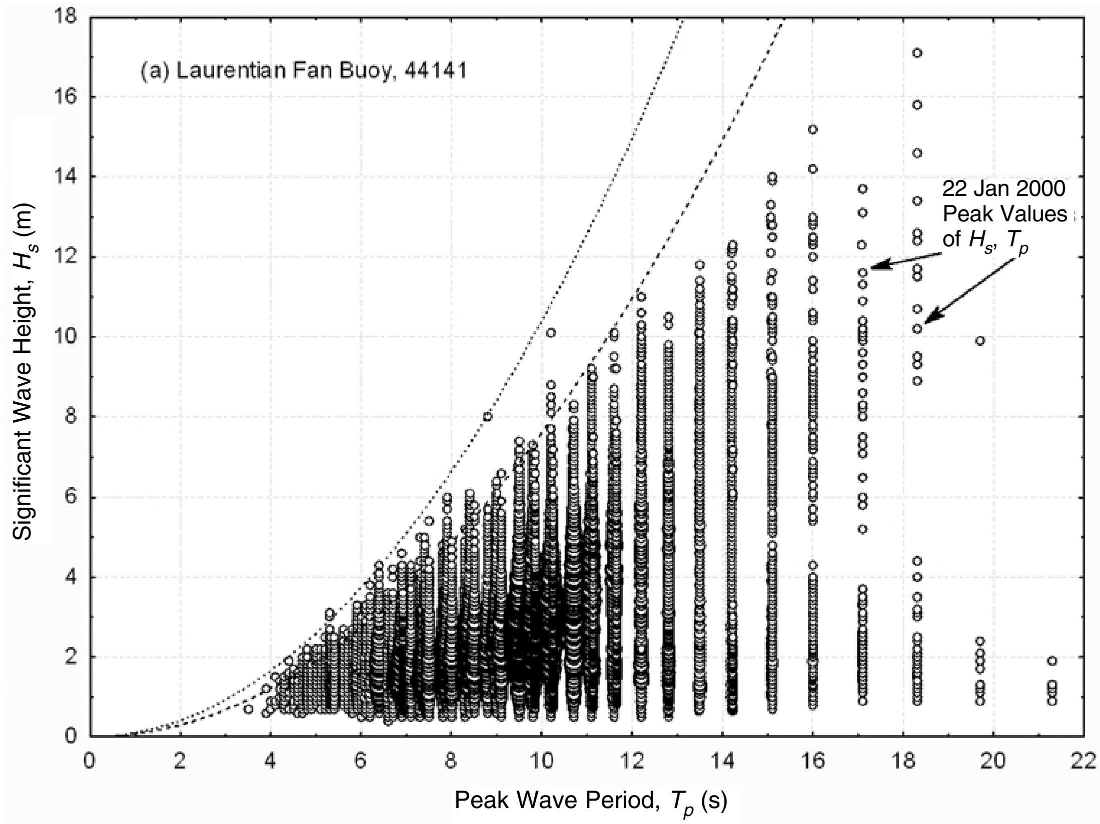

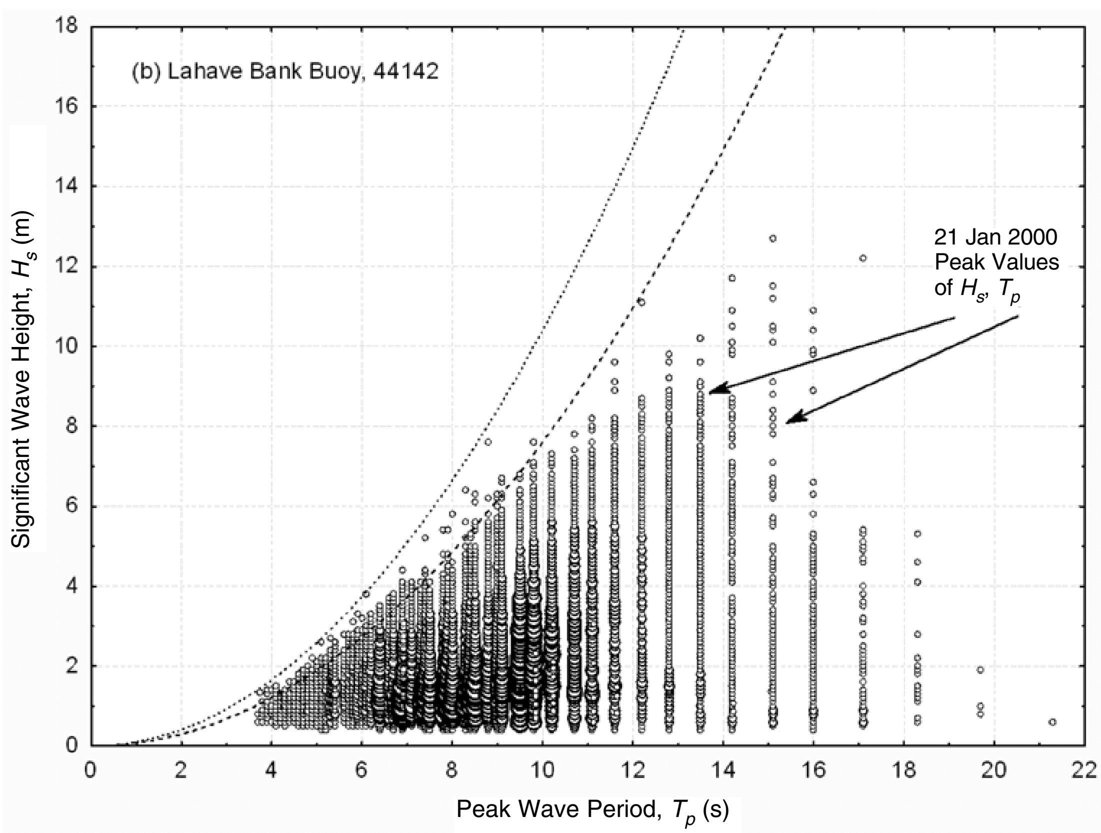

Fig. 13 Joint frequency distribution of significant wave height, H_s, and peak wave period, T_p, for the 14-year record September 1990 – January 2005 for (a) the Laurentian Fan buoy, 44141, and (b) the Lahave Bank buoy, 44142. The dotted line indicates a wave steepness of 1:15 and the dashed line that of 1:20.5. Arrows indicate the peak H_s with the corresponding T_p and the maximum T_p with the corresponding H_s at each buoy during the 20–22 January 2000 storm.

winds are validated against available NDBC and MSC buoy observations. The significant wave height and peak period used in this study are those reported by the buoys. In the case of the MSC buoys, the reported values are used as opposed to the values recalculated by MEDS from the transmitted 1-d spectra derived from FFT analysis of the raw buoy data.

The model validation indicates that SWAN using WAM3 physics performs better than the WAM4 physics as implemented in SWAN, which confirms the findings of Booij et al. (1999), Lalbeharry (2002) and Lalbeharry et al. (2004). However, the modified version of the SWAN implementation of WAM4 produces wave results that are more accurate than those of the unmodified version and are in closer agreement with those using the WAM3 option of SWAN, results that are consistent with those of Lalbeharry et al. (2004). The improved significant wave height from the SWN-WAM4+ run is ascribed to the modifications made to the SWAN WAM4 since other factors such as source terms, numerical schemes, winds and grid resolutions in the two SWAN runs are identical. The coarse and nested fine grid WAM4.5 produce results that show minimal differences suggesting that in deep and intermediate water depths represented by the observations used in this study, the coarse grid WAM4.5 with a grid resolution of 0.5° can be used in operational applications. However, unresolved small islands and submerged bathymetric features in the coarse grid area may have an effect on the model waves generated and on the wave propagation (Janssen et al., 2005). The agreement between the peak H_s of the SWN-WAM4+ run and that of the WAM45-FG is reasonably good at buoy locations where the sea is locally wind-sea dominated and not so good where the sea state is swell dominated. The factors most likely to contribute to the latter disagreement are the propagation scheme used by SWAN in non-stationary mode in which the so-called garden-sprinkler effect may show up for swell propagation over large distances and the difference in the swell separation methods used by SWAN and WAM4.5.

The three model runs overpredict the peak H_s at buoy 44141 at 12:00 UTC on 21 January and that at buoy 44255 at 09:00 UTC on 22 January. In the former case the overprediction is linked to the local wave steepness reaching a value close to the limiting value before breaking. In the latter case, it appears that dynamic fetch exists in the model space and is the likely mechanism contributing to the overestimation of the peak, unlike the mechanism suggested for the model overprediction of the peak H_s at buoy 44141.

Two exceptionally large individual waves with an H_{max} estimated to be close to 16 m and an H_s approximately 10 m struck the Channel Head area of Port-aux-Basques around 06:30 UTC on 22 January. The model 12 m wave height contour arrives in the Channel Head area around 06:30 UTC, the same arrival time as the first of the two big waves. The simulation by the wave model of such extreme wave height arriving around the same time as the big wave, therefore, lends credence to the likelihood of the occurrence of the two so-called 'freak' waves generated by this storm.

The model scatter plots of wave heights reveal that both the coarse and fine grids of WAM4.5 do a better job than SWAN in predicting wave heights in excess of 5 m. The wave height statistics confirm the better performance of the SWN-WAM4+ version over that of the SWN-WAM4 version and the minimal difference between the coarse and fine grid versions of WAM4.5. Overall, the two wave models used in this study, in particular WAM4.5, perform reasonably well in simulating the extreme sea states for this storm case. The observed combination of extreme H_s and long wave periods occurs infrequently in the 14-year wave record at the two Scotian Shelf buoy locations.

Acknowledgements

The authors wish to express their sincere thanks to SEIMAC Limited, Dartmouth, NS and COA Coastal Ocean Associates Inc. for providing waverider data from oil and gas platforms operating near Sable Island. Other archived wave data were provided by the Marine Environmental Data Service, Fisheries and Oceans, Canada and the NOAA National Data Buoy Centre. The reviewers are also acknowledged for their helpful comments and suggestions which led to significant improvements in the paper.

Appendix: Description of statistical parameters

bias = $1/N\Sigma(Y_i - X_i)$ is the mean error

rmse = $[1/N\Sigma(Y_i - X_i)^2]^{1/2}$ is the root mean square error of the deviations

SI = rmse/(Buoy Mean) is the scatter index

r = $[1/N\Sigma(Y_i - Y_{mean})(X_i - X_{mean})]/\sigma_y\sigma_x$ is the linear correlation coefficient

ac = $\Sigma(Y_i - X_c)(X_i - X_c)/[\Sigma(Y_i - X_c)^2(X_i - X_c)^2]^{1/2}$ is the anomaly correlation

rv = $1 - \Sigma(Y_i - X_i)^2/\Sigma(X_i - X_c)^2$ is the reduction of variance

b = slope and a = y-intercept of the best fit linear regression line

where X_i and Y_i are, respectively, the i^{th} observed and model values, X_c is the climatology of X defined here as the mean of all the buoy observations, σ_y is the standard deviation of Y, σ_x is the standard deviation of X and N is the number of observations.

References

AXYS ENVIRONMENTAL CONSULTING LTD. 1996. Meteorological and oceanographic measurements from the Canadian weather buoys. A review of sensors, data reduction, transmission, quality control and archival methods. Final report for Environment Canada, Downsview, Ontario, April 1996. Available from MEDS.

AXYS ENVIRONMENTAL SYSTEMS. 2000. The Canadian buoy network technical meeting. A review of sea surface temperature measurements, metadata, and wave sensing and processing. Summary report and action items prepared for Environment Canada, Downsview, Ontario, February 2000.

BERGLAND, G. D. 1969. Guided tour of the fast Fourier transform. IEEE Spectrum, **6**: 41–52.

BIDLOT, J.-R.; D. J. HOLMES, P. A. WITTMANN, R. LALBEHARRY and H. S. CHEN. 2002. Intercomparison of the performance of operational ocean wave forecasting systems with buoy data. *Weather Forecast.* **17**: 287–310.

BIGIO, R. 1996. Significant and extreme waves generated by hurricane Luis as observed by Canadian meteorological buoys and the Cunard cruise ship Queen Elizabeth 2. *CMOS Bull.* **24**: (5): 112–117.

Bobanovic, J.; K. R. Thompson, S. Desjardins and H. Ritchie. 2006. Forecasting storm surges along the East Coast of Canada and the northeastern United States: The storm of 21 January 2000. ATMOSPHERE-OCEAN, **44** (2): 151–161.

BOOIJ, N.; R. C. RIS and L. H. HOLTHUIJSEN. 1999. A third generation wave model for coastal regions 1. Model description and validation. *J. Geophys. Res*. **104** (C4): 7649–7666.

BORGEL, D. 2001. January 21, 2000 Storm: The forecasting challenges and impact on the oil and gas operations near Sable Island. *In*: Proc. International Workshop on Operational Marine Forecasting, 18-22 November 2001, Dartmouth, NS, Canada. Electronic presentation published on CD by Environment Canada.

BOWYER, P. J. and A. W. MACAFEE. 2005. The theory of trapped-fetch waves with tropical cyclones - An operational perspective. *Weather Forecast.* **20**: 229–244.

BUCKLEY, W. H. 1988. Extreme and climatic wave spectra for use in structural design of ships. *Naval Eng. J.* **100**: 36–58.

CARDONE, V. J.; H. C. GRABER, R. E. JENSEN, S. HASSELMANN and M. J. CARUSO. 1995. In search of the true surface wind field in SWADE IOP-1: Ocean wave modeling perspective. *Global Atmos. Ocean Sys.* **3**(2-3): 107–150.

CAVALERI, L. and P. MALANOTTE-RIZZOLI. 1981. Wind wave prediction in shallow water: Theory and applications. *J. Geophys. Res*. **86**: 10961–10973.

DATAWELL BV. 2006. Datawell waverider reference manual. Datawell BV, Zumerlustraat 4, 2012 LM Haarlem, The Netherlands, 21 July 2006.

DURANT, T. H. and D. GREENSLADE. 2007. Validation and application of Jason-1 and Envisat wave heights. *In*: Proc. 10th Int. Workshop on Wave Hindcasting and Forecasting and Coastal Hazard Symposium, North Shore, Oahu, Hawaii, 11–16 Novembe 2007. Available on CD from Environment Canada.

EARLE, M. D. 1996. Nondirectional and directional data analysis procedures. NDBC Technical Document 96-01, Stennis Space Center, January 1996.

FORBES, D.; G. PARKES, C. O'REILLY, R. DAIGLE, R. TAYLOR, N. CATTO, M. CAMPBELL and L. KETCH. 2000. Storm surge, sea-ice and wave impacts of the 21-22 Jan. 2000 storm in coastal communities of Atlantic Canada. *In*: Proc. Canadian Meteorological and Oceanographic Society 34th Annual Congress, 29 May – 2 June 2000, Victoria, British Columbia.

HASSELMANN, K.; T. P. BARNETT, K. BOUWS, H. CARLSON, D. E. CARTWRIGHT, K. ENKE, J. I. EWING, H. GIENAPP, D. E. HASSELMANN, P. KRUSEMAN, A. MEERBURG, P. MULLER, K. RICHTER, D. J. OLBERS, W. SELL and H. WALDEN. 1973. Measurements of wind-wave growth and swell decay during the Joint North Sea Wave Project (JONSWAP). *Dtsch. Hydrogr. Z.* **A8**(12): 1–95.

HASSELMANN, S.; K. HASSELMANN, J. H. ALLENDER and T. P. BARNETT. 1985. Computations and parameterizations of the nonlinear energy transfer in a gravity-wave spectrum. Part II: Parameterizations of the nonlinear transfer for application in wave models. *J. Phys. Oceanogr.* **19**: 745–754.

HERSBACH, H. and P. A. E. M. JANSSEN. 1999. Improvement of the short-term behaviour in the wave ocean model (WAM). *J. Atmos. Oceanic Technol*. **16**: 884–892.

HOLTHUIJSEN, L. H. 2007. *Waves in Oceanic and Coastal Waters*. Cambridge University Press, Cambridge, 387 pp.

JANSSEN, P. 1989. Wave-induced stress and the drag of air flow over sea waves. *J. Phys. Oceanogr*. **19**: 745–754.

JANSSEN, P. 1991. Quasi-linear theory of wind-wave generation applied to wave forecasting. *J. Phys. Oceanogr*. **21**: 1631–1642.

JANSSEN, P.; B. HANSEN and J. R. BIDLOT. 1997. Verification of the ECMWF wave forecasting system against buoy and altimeter data. *Weather Forecast.* **12**: 763–784.

JANSSEN, P.; J.-R. BIDLOT, S. ABDALLA and H. HERSBACH. 2005. Progress in ocean wave forecasting at ECMWF. ECMWF Tech. Memo., 478. ECMWF, Reading, U.K., 27 pp. Available online at http://www.ecmwf.int/publications/

JENSEN, R. E.; V. J. CARDONE and A. T. COX. 2006. Performance of third generation wave models in extreme hurricanes. *In*: Proc. 9th Int. Workshop on Wave Hindcasting and Forecasting, Victoria, British Columbia, Canada, 24–29 September 2006. Available on CD from Environment Canada.

KOMEN, G. J.; S. HASSELMANN and K. HASSELMANN. 1984. On the existence of a fully developed windsea spectrum. *J. Phys. Oceanogr*. **14**: 1271–1285.

KOMEN, G. J.; L. CAVALERI, M. DONELAN, K. HASSELMANN, S. HASSELMANN and P. A .E. M. JANSSEN. 1994. *Dynamics and Modelling of Ocean Waves*. Cambridge University Press, Cambridge, 532 pp.

LALBEHARRY, R. 2002. Comparison of the performances of three state-of-the-art ocean wave models in extreme storm cases. *In*: Proc., 7th Int. Workshop on Wave Hindcasting and Forecasting, Banff, Alberta, 21–25 October 2002. Published by Environment Canada.

LALBEHARRY, R.; A. BEHRENS, H. GUENTHER and L. WILSON. 2004. An evaluation of wave model performances with linear and nonlinear dissipation source terms in Lake Erie. *In*: Proc., 8th Int. Workshop on Wave Hindcasting and Forecasting, North Shore, Oahu, Hawaii, 14–19 November 2004. Available on CD from Environment Canada.

MACAFEE, A. W. and P. J. BOWYER. 2005. The modeling of trapped-fetch waves with tropical cyclones - A desktop operational model. *Weather Forecast.* **20**: 245–263.

MONBALIU, J.; R. PADILLA-HERNANDEZ, J. C. HARGREAVES, J. C. ALBIACH, W. LUO, M. SCLAVO and H. GUENTHER. 2000. The spectral wave model, WAM, adapted for applications with high resolution. *Coastal Eng.* **41**: 41–62.

PARKES, G. S. and L. A. KETCH. 2002. Appendix 1, Part 2: Storm-surge climatology. Coastal Impacts of Climate Change and Sea-Level Rise on Prince Edward Island. M. McCulloch, D. Forbes and R. Shaw (Eds). CCAF Technical Report, Geological Survey of Canada, Open File 4261.

PERRIE, W.; E. L. ANDREAS, W. ZHANG, W. LI, J. GYAKUM and R. MCTAGGART-COWAN. 2005. Sea spray impacts on intensifying midlatitude cyclones. *J. Atmos. Sci*. **62**: 1867–1883.

PIERSON, W. J. and L. MOSKOWITZ. 1964. A proposed spectral form for the fully developed wind seas based on the similarity theory of S. A. Kitaigorodskii. *J. Geophys. Res.* **69**: 5181–5190

RIS, R. C. 1997. Spectral modelling of wind waves in coastal areas. PhD Thesis, Delft University of Technology, Delft, the Netherlands.

RIS, R. C.; L. H. HOLTHUIJSEN and N. BOOIJ. 1999. A third generation wave model for coastal regions 2. Verification. *J. Geophys. Res.* **104**(C4): 7667–7681.

SANDERS, F. and J.R. GYAKUM. 1980. Synoptic-dynamic climatology of the "bomb." *Mon. Weather Rev.* **108**: 1589–1606.

SKEY, S. G. P.; K. BERGER-NORTH and V. R. SWAIL. 1998. Measurement of winds and waves from a NOMAD buoy in high seas. *In*: Proc., 5th Int. Workshop on Wave Hindcasting and Forecasting, Melbourne, Florida, 26–30 January 1998. Published by Environment Canada.

SKEY, S. G. P.; K. BERGER-NORTH, V. R. SWAIL and A. CORNETT. 1999. The storm wind studies (SWS). CLIMAR 99, WMO Workshop on Advances in Marine Climatology, 8–15 September 1999, Vancouver, Canada.

SWAN. 2004. User Manual SWAN Cycle III version 40.31, 5 February 2004. Delft University of Technology, Department of Civil Engineering, the Netherlands.

THOMPSON, K. R.; H. RITCHIE, N.B. BERNIER, J. BOBANOVIC, S. DESJARDINS, P. PELLERIN, W. BLANCHARD, B. SMITH and G.S. PARKES. 2002. Supporting Document 5: Modelling storm surges and flooding risk at Charlottetown. Coastal Impacts of Climate Change and Sea-Level Rise on Prince Edward Island. M. McCulloch, D. Forbes and R. Shaw (Eds). CCAF Technical Report, Geological Survey of Canada, Open File 4261.

TOLMAN, H. J. 1992. Effects of numerics on the physics in a third generation wind-wave model. *J. Phys. Oceanogr*. **22**: 1095–1111.

WAMDI GROUP. 1988. The WAM model - A third generation ocean wave prediction model. *J. Phys. Oceanogr*. **18**: 1775–1810.

WMO (WORLD METEOROLOGICAL ORGANIZATION). 1998. Guide to Wave Analysis and Forecasting. WMO-No. 702. 2nd ed. 159 pp.